

# Measurement Report: Cloud and environmental properties associated with aggregated shallow marine cumulus and cumulus congestus

Ewan Crosbie<sup>1,2</sup>, Luke D. Ziemba<sup>1</sup>, Michael A. Shook<sup>1</sup>, Taylor Shingler<sup>1</sup>, Johnathan W. Hair<sup>1</sup>, Armin Sorooshian<sup>3,4</sup>, Richard A. Ferrare<sup>1</sup>, Brian Cairns<sup>5</sup>, Yonghoon Choi<sup>1,2</sup>, Joshua DiGangi<sup>1</sup>, Glenn S. Diskin<sup>1</sup>, Chris Hostetler<sup>1</sup>, Simon Kirschler<sup>6,7</sup>, Richard H. Moore<sup>1</sup>, David Painemal<sup>1,2</sup>, Claire Robinson<sup>1,2,\*</sup>, Shane T. Seaman<sup>1</sup>, K. Lee Thornhill<sup>1,2</sup>, Christiane Voigt<sup>6,7</sup>, Edward Winstead<sup>1,2</sup>

<sup>1</sup>NASA Langley Research Center, Hampton, VA 23666, U.S.A.

<sup>2</sup>Analytical Mechanics Associates, Inc., Hampton, VA 23666, U.S.A.

<sup>3</sup>Department of Chemical and Environmental Engineering, University of Arizona, Tucson, AZ 85718, U.S.A.

<sup>4</sup>Department of Hydrology and Atmospheric Sciences, University of Arizona, Tucson, AZ 85718, U.S.A.

<sup>5</sup>NASA Goddard Institute for Satellite Studies, New York, NY 10025, U.S.A.

<sup>6</sup>Institut für Physik der Atmosphäre, Deutsches Zentrum für Luft- und Raumfahrt (DLR), Oberpfaffenhofen, Germany

<sup>7</sup>Institut für Physik der Atmosphäre, Johannes Gutenberg-Universität, Mainz, Germany

\* deceased

*Correspondence to:* Ewan Crosbie (ewan.c.crosbie@nasa.gov)

## Abstract.

Mesoscale organization of marine convective clouds into linear or clustered states is prevalent across the tropical and subtropical oceans and its investigation served as a guiding focus for a series of process study flights, conducted as part of the Aerosol Cloud Meteorology Interactions over the western Atlantic Experiment (ACTIVATE) during summer 2020, 2021 and 2022. These select ACTIVATE flights involved a novel strategy for coordinating two aircraft, with respective remote sensing and in situ sampling payloads, to probe regions of organized shallow convection for several hours. The main purpose of this measurement report is to summarize the aircraft sampling approach, describe the characteristics and evolution of the cases, and provide an overview of the datasets that can serve as a starting point for more detailed modeling and analysis studies.

Six flights are described, involving a total of 80 dropsonde profiles that capture the environment surrounding clustered shallow convection together with detailed observations of the vertical structure of cloud systems, comprising up to 20 altitude levels that were sampled in situ. Four cases involved deepening convection rooted in the marine boundary layer that developed vertically to 2-5 km with varying precipitation amounts, while two cases captured more complex and developed cumulus congestus systems extending above 5 km. In addition to the thermodynamic and dynamic characterization afforded by dropsonde and in situ measurements, the datasets include cloud and aerosol microphysics, trace gas concentrations, aerosol and droplet composition, and cloud and aerosol remote sensing from high spectral resolution lidar and polarimetry.

## 1 Introduction

Cumulus convection is a pervasive component of the marine atmosphere above the global tropical and subtropical oceans (Warren et al., 1988; Johnson and Lin, 1997; Bony et al., 2004) where vertical transport and overturning circulations are tightly coupled to diabatic processes associated with radiative and latent heating (Riehl and Malkus, 1958; Johnson et al., 1999; Sobel and Bretherton, 2000). In addition to their role in the heat, moisture, and momentum budgets, convective clouds across all scales affect the production, loss, and vertical distribution of atmospheric trace gases (e.g., Dickerson et al., 1987; Fried et al., 2016; Li et al., 2018) and aerosol particles (e.g., Koch et al., 2003; Berg et al., 2015; Corr et al., 2016; Wonaschuetz et al., 2012; Reid et al., 2019; Leung and van den Heever, 2022). Tropical cloudiness has been associated with three major modes (Johnson et al. 1999; Haynes and Stephens, 2007): (i) a shallow cumulus mode, often capped by a trade wind inversion, (ii) a middle mode associated with cumulus congestus and altocumulus, often associated with enhanced stability near the melting level (Posselt et al., 2008), and (iii) a deep mode (not considered here) associated with cumulonimbus and anvil cirrus, capped by the tropopause.

Oceanic regions that frequently accommodate deep convection are also subject to suppressed periods with shallow convection (Johnson and Lin, 1997; Malkus and Riehl, 1964). The vertical distribution and extent of clouds in unstable environments capable of supporting deep convection are also strongly dependant on the moisture profile (Redelsperger et al., 2002; Jensen and Del Genio, 2006; Takayabu et al., 2006) because of the inhibiting influence of entrainment and mixing on updraft buoyancy (Derbyshire et al., 2004). Indeed, pre-moistening of the mid-troposphere (Kuang and Bretherton 2006; Waite and Khouider, 2010) and upscaling of cloud-forming updrafts (e.g., through cold pools, Khairoutdinov and Randall, 2006), as well as moisture convergence (Hohenegger and Stevens, 2013), have been thought necessary to facilitate the growth from shallow to deep convection. For thermodynamic environments that lack pronounced stable layers (e.g., a demarcated cloud-capping trade-wind inversion), separation of the shallow cumulus mode from growth into congestus may be more ambiguous and resigned to a subjective altitude threshold (e.g., 3-4 km). Similarly, a subset of clouds identified or classified as congestus may encompass nascent energetic growth of transient systems on their way to becoming deep convection (e.g., Luo et al., 2009), which may physically differ from terminal congestus, where development has ceased (Leung and van den Heever, 2022).

In addition to understanding factors that control the vertical distribution of cumulus clouds, there has been a surge of recent interest in the spatial distribution of convection, particularly spurred by the propensity for deep and shallow convection to self-aggregate in cloud resolving models under certain conditions. Simulations run close to a state of radiative-convective equilibrium over a homogeneous ocean surface can produce deep convection that progressively self-aggregates (Held et al., 1993; Tompkins, 2001; Tompkins and Craig, 1998; Bretherton et al., 2005; Muller and Held, 2012; Wing and Emanuel, 2014) and mimics the tendency for oceanic convection in the real tropical atmosphere to structurally organize across a wide range of horizontal length scales (Holloway et al., 2017; Mapes and Houze, 1993; Zuidema 2003; Stein et al., 2017; Tobin et

al., 2012; Semie and Bony, 2020; Masunaga, 2014; Nesbitt et al., 2006). Large eddy simulations (LES) of shallow marine cumulus have been found to exhibit similar mesoscale self-aggregation of moisture and cloudiness, attributed purely to moisture advection and negative gross moist stability through model experiments that suppressed interactive radiation, surface fluxes, and precipitation (Bretherton and Blossey, 2017; Narenpitak et al., 2022; Janssens et al., 2023). In contrast, using LES experiments replicating conditions encountered during the Rain in Cumulus over the Ocean experiment (RICO; Rauber et al., 2007), Seifert and Heus (2013) found that cold pools from shallow cumulus precipitation were necessary to produce the cloud organization into mesoscale arcs. Furthermore, shipboard observations during RICO confirmed the presence of frequent convective showers associated with shallow cumulus and their accompanying cold pools (Zuidema et al., 2012). Linkages have been made between precipitation-mediated shallow cloud organization and the influence of aerosols in modelling studies (Xue et al., 2008; Wang et al., 2010) and observations (Wood et al., 2018; Mohrmann et al., 2019; Goren et al., 2019). A wide spectrum of shallow cloud organization types have been identified in nature ranging from patterns found in stratocumulus (e.g., Wood and Hartmann, 2006), organization in mid-latitude cold air outbreaks (Agee 1987, Atkinson and Zhang, 1996), fair weather cumulus rolls (Lemone and Meitin, 1984), cloud patterns found in deeper boundary layers of the downstream trades (Schulz et al., 2021; Denby 2020; Stevens et al., 2020; Janssens et al., 2021), and those associated with cold pools and congestus (Snodgrass et al., 2009; Zuidema et al., 2012; Rowe and Houze, 2015; Ruppert and Johnson, 2015). There is a clear need for continued observational efforts focused on cumulus aggregation to test and/or verify the findings from idealized numerical model simulations and provide detailed observational support for the driving physical and dynamical processes across these various regimes.

Shallow cumulus clouds modulate albedo and changes in their fractional coverage, vertical extent, and microphysical properties can exert a strong influence on regional and global climate (Bony et al., 2004; Vial et al., 2016; Rieck et al., 2012). In addition, the response of low-lying shallow cumulus, particularly in the trade wind regions, to climate warming constitutes a sizable uncertainty in climate model cloud feedbacks (Bony and Dufresne, 2005; Bretherton 2015; Bretherton et al., 2013; Sherwood et al., 2014; Webb and Lock 2013). The amount of cloud coverage near cloud base (i.e., resulting from the contributions of very small cumulus) dominates the overall cloud fraction (Nuijens et al., 2014). Increases in convective mixing, driven by increased mass flux in deeper, active cumulus, projected to occur in future warming (Vial et al., 2016), has been postulated to result in desiccation of neighbouring small clouds by entrainment drying (Brient and Bony, 2013; Sherwood et al., 2014; Brient et al., 2015), thus reducing the cloud base cloud fraction. However, recent analysis of trade-wind cumulus observations has cast doubt on the strength of this feedback (Vogel et al., 2022), suggesting the importance of mesoscale organization of these clouds and ubiquitous low-level mesoscale overturning circulations that drives the distribution of cloudiness (George et al., 2023). Variations in the type of mesoscale organization has been shown to result in changes in fractional coverage of shallow clouds and resultant cloud radiative effects (e.g., Bony et al., 2020), motivating the need for process-level understanding and effectual realization of their associated properties in climate models.

Microphysical properties of warm (ice free) cumulus are controlled, in part, by the availability of aerosol particles to act as cloud condensation nuclei (CCN) and by dynamics (Kirschler et al., 2022). Clouds forming in higher CCN environments

100 result in smaller cloud droplets for fixed liquid water content (Twomey, 1977) that may delay and/or suppress the formation  
of precipitation (e.g., Rosenfeld and Lensky, 1998; Khain et al., 2005) and affect how cloudy parcels interact with their  
environment (e.g., Xue and Feingold, 2006). Retained cloud water and changes to the condensation rate may affect updraft  
buoyancy in competing ways (Igel and van den Heever, 2021; Grabowski and Morrison, 2021; Fan et al., 2018), affecting  
both shallow clouds that remain liquid only (e.g., Koren et al., 2014) and the potential for invigoration in the ice phase (e.g.,  
105 Rosenfeld et al., 2008). In concert, these aerosol-mediated changes may influence the timeline of cloud growth, coverage,  
vigor, terminal vertical extent, and lifecycle precipitation (Koren et al., 2005; Koren et al., 2008; Tao et al., 2012; Igel and  
van den Heever, 2021; Barthlott et al., 2022; Fan et al., 2018; Rosenfeld et al., 2008; Storer and van den Heever, 2013;  
Khain et al., 2005; Marinescu et al., 2021).

Lateral and vertical mixing processes involving interactions between clouds and the surrounding environment are ubiquitous  
110 (Romps and Kuang, 2010) and exert control on the vertical distribution of cloud water (Rangno and Hobbs, 2005).  
Entrainment of subsaturated environmental air may influence the droplet population differently depending on the relative  
timescales of turbulent homogenization and microphysical response (Baker et al., 1980; Burnet and Brenguier, 2007; Jensen  
and Baker, 1989), which is a function of both the droplet sizes and the length scales of mixing (Kumar et al., 2018). The  
spatial and temporal heterogeneity of clouds, precipitation, and aerosols (and feedbacks therein) confounds efforts to  
115 understand aerosol-cloud interactions (Gryspeerd et al., 2015; Varble et al., 2018), while aerosol effects on cloud  
microphysics may be modulated by the environment (Storer et al., 2010; Sokolowsky et al., 2022). Clouds also mediate the  
microphysical properties of subsequent clouds through their influence on pre-existing CCN properties (Hoppel et al., 1994;  
Feingold and Kreidenweis, 2000), the removal of CCN by rainout (Textor et al., 2006; Wang et al., 2020; Flossman et al.,  
1985) and the lofting of precursor gases that nucleate new particles (Williamson et al., 2019). In summary, the myriad multi-  
120 path interactions amongst aerosols, clouds, radiation, and meteorology from the cloud system to the droplet scale may all  
contribute to the complexity of mesoscale aggregation of marine cumulus and motivate the need for targeted observations  
and further modelling.

In this paper, we present observational case studies associated with targeted aircraft measurements of aggregated shallow  
cumulus and terminal cumulus congestus that were conducted over the summertime subtropical western North Atlantic near  
125 the coastal United States and Bermuda. Although this region is situated near the latitudinal extent of the tropics, sea surface  
temperatures (SST) are at a range close to typical of tropical basins (298-300 K) and low-level warm, moist advection driven  
by flow around the subtropical ridge produces airmasses that are thermodynamically similar to conditions found in tropical  
maritime regions. These cases encompass a variety of mesoscale cloud conditions, exemplified by the nature of cloud  
organization and aggregation, vertical extent, macro- and microphysical properties, and environmental attributes, while  
130 occurring under relatively consistent larger scale environments. The measurements include both in situ and remote sensing  
datasets from two coordinated aircraft platforms that specifically targeted regions of aggregated shallow convection. The  
main purpose of this measurement report is to summarize the aircraft sampling approach, describe the characteristics and

evolution of the cases, and provide an overview of the datasets that can serve as a starting point for more detailed modeling and analysis of this set of case studies.

## 135 **2 Methods and Datasets**

### **2.1 ACTIVATE**

The Aerosol Cloud meTeorology Interactions oVer the western ATlantic Experiment (ACTIVATE) was conducted from NASA Langley Research Center and Bermuda during 2020-2022, comprising six airborne measurement campaigns split between winter and summer each year (Sorooshian et al., 2019). ACTIVATE employed a unique coordinated aircraft strategy for remote sensing and in situ sampling of clouds, aerosols, and trace gases that involved speed matching a turboprop King Air B200 or UC12 (King Air) at high altitude with a low-flying Dassault HU-25 Falcon jet (Falcon) allowing both aircraft to remain horizontally collocated. Most flights used the coordinated aircraft in a survey pattern to build statistics (e.g., Kirschler et al., 2023), while a minority of flights were assigned to process studies during each season. During summer, process study flights were used specifically to probe organized regions of aggregated shallow cumulus and cumulus congestus, which was a regularly occurring cloud pattern observed across the region.

145 Unlike statistical surveys where both aircraft prioritized following a single path, summer process study flights prescribed separate, but coordinated, patterns for each aircraft that were anchored to a target cloud system or convective feature (Figure 1). At a nominal cruise altitude of 9 km, the King Air flew at least five transects across the target on different azimuths connected by shorter perimeter legs. Each transect covered nominally 80 km with dropsondes released near the start and end of each transect to create a perimeter, as well as occasional placements near the center. Meanwhile, the Falcon performed a series of short, constant altitude penetrations of the target cloud system and the near-field environment, repeated at multiple levels that also included a leg just above the highest cloud top and at least one leg below the lowest cloud base. Legs that penetrated cloud began close to cloud top, where there was typically a single emergent convective core, then progressively moved down in altitude, usually resulting in longer sampling legs as the cloudy region expanded to involve multiple cores, as illustrated schematically in Figure 1a. The Falcon sampled the vertical structure of the surrounding environment, including one profile flown as a spiral located in a region completely free from any cloud, when possible.

155 A total of six process studies comprising individual research flights (RF) were conducted using this flight module design: (1) RF39 2020-09-29, (2) RF77 2021-06-02\_L2, (3) RF80 2021-06-07\_L2, (4) RF171 2022-06-10\_L2, (5) RF173 2022-06-11\_L2, and (6) RF176 2022-06-14 (Note: following the archiving convention L2 denotes the second flight of a given day).  
160 Here we will describe these respective flights as Cases 1-6. Cases 1-3 were flown from NASA Langley Research Center and Cases 4-6 were flown from Bermuda, where the project was based during June 2022. The flights originating from Bermuda benefitted from fewer airspace restrictions and shorter transit times to regions of interest resulting in longer loiter times for sampling. Consequently, Case 4 included a second cloud target that was fully sampled by the Falcon but partially sampled by the King Air without additional dropsondes. Case 5 comprised two modules that included both aircraft, but the initial

165 module was abbreviated by the Falcon because of rapid decay of the targeted cloud system. For instances where we wish to  
differentiate the two sections of these flights, they will be referred to as Case 4A/B and 5A/B, respectively. Cases 1 and 6  
occurred earlier in the day with module midpoints approximately an hour prior to local solar noon (15-16 UTC) while Cases  
2-5 were later occurring approximately 2-4 hours after local solar noon (18-20 UTC) as a result of being the second flight of  
a two-flight day).

## 170 **2.2 King Air**

A multi-wavelength airborne high spectral resolution lidar (HSRL-2; Hair et al., 2008; Burton et al., 2018) provided  
vertically resolved aerosol and cloud properties below the King Air altitude. The HSRL-2 generates simultaneous  
measurements of particle backscatter coefficient and depolarization ratio at 355, 532, and 1064 nm as well as particle  
extinction coefficient at 355 and 532 nm, providing information about aerosol extensive and intensive properties. Aerosol  
175 type (marine, polluted marine, pure dust, dusty mix, smoke, fresh smoke, and urban) was derived using the depolarization  
ratio, spectral depolarization ratio, color ratio, and lidar ratio (Burton et al., 2012, Burton et al., 2014). Particle backscatter  
was used to diagnose the presence of liquid clouds and determine cloud top height at high vertical (~1.25 m) and horizontal  
(~60 m) resolution.

The Research Scanning Polarimeter (RSP) is a passive downward facing polarimeter with nine spectral bands (410, 470,  
180 550, 670, 865, 960, 1590, 1880, and 2260 nm) that scans along the direction of flight (nadir  $\pm 55^\circ$ ) providing retrievals of  
aerosol, cloud, and surface properties (Cairns et al., 2003). During conditions with a narrow viewing angle differential  
relative to the solar principal plane and absence of cirrus, the RSP was used to provide cloud top microphysical properties  
including the drop size distribution for liquid clouds (Alexandrov et al., 2018).

The NCAR Airborne Vertical Atmospheric Profiling System was included on the King Air to acquire dropsonde  
185 observations, providing vertical profiles of temperature, humidity, pressure, and horizontal wind components. The  
dropsondes used here were the NCAR NRD41 “mini-sondes” (Vömel et al., 2021, Vömel et al., 2023).

A nadir-facing camera (Case 1: Garmin VIRB Ultra 30 and Cases 2-6: AXIS F-1005-E) was mounted underneath the  
fuselage to provide continuous (1-2s frame rate) images of the cloud scene. The AXIS camera was fitted with different  
lenses that changed the field of view amongst cases resulting in a different footprint when viewed from 9 km. The camera  
190 images were also used to qualitatively diagnose the position of the aircraft during transects with respect to the target cloud  
system.

## **2.3 Falcon**

Full details and specifications of the Falcon payload are described in Sorooshian et al. (2023) and here we provide a  
summary of the instruments. Water vapor was measured using an open path Diode Laser Hygrometer (Diskin et al., 2002)  
195 and temperature was obtained from measurements of total air temperature using a Rosemount 102 probe. Three-dimensional  
wind components were derived using a radome-mounted, inertially-corrected 5-hole gust probe (Thornhill et al., 2003;

Barrick et al., 1996). Temperature, water vapor, and winds were acquired at 20 Hz. CO, CO<sub>2</sub> and CH<sub>4</sub> were measured using a near-IR cavity ringdown spectrometer (Picarro G2401-m; DiGangi et al., 2021) and O<sub>3</sub> was measured by a dual-beam ultraviolet absorption sensor (2B Technologies, Model 205), all at ~2 s sampling interval.

200 Cloud droplet size distributions (DSD) were measured [at 1 Hz](#) using a Fast Cloud Droplet Probe (FCDP; SPEC Inc.) and a 2D-S Probe (SPEC Inc.; Lawson et al., 2006) spanning 3-50 μm and 30-1500 μm drop diameter, respectively. The distributions from both instruments were merged [at 1 Hz](#) onto a uniform logarithmic grid (smoothed to 20 bins per decade) and a weighted average taken in the overlap region (30-50 μm), with weights smoothly transitioning from FCDP to 2D-S. The linear spaced size grid for the 2D-S, based on pixel occultation, results in low counting statistics for larger drops and is improved by re-binning. During Cases 1 and 2, there were some periods where 2D-S data were not acquired and precipitation DSD data from the Cloud Imaging Probe (CIP; Droplet Measurement Technologies) were substituted covering the size range 500-1500 μm, which represented the only range where image analysis could be conducted for the CIP. Thus, during these periods no DSD data in the 50-500 μm range could be derived.

210 All clouds sampled by the Falcon in these process studies contained only liquid drops, as verified using particle imagery supplied by the 2D-S. The number concentration, N<sub>d</sub>, liquid water mixing ratio, q<sub>L</sub>, and precipitation rate were determined through integration of the DSD and terminal velocity data from Beard (1976), since in situ samples were verified as liquid drops. A notable caveat in relation to cloud phase exists for Case 6 where liquid-only supercooled drops at ~-8°C were observed near cloud top (~5.6 km) at the time of initial Falcon sampling. The Falcon progressed downward in altitude to warmer temperatures while continuing to observe liquid-only conditions, but the cloud system was concurrently observed by the King Air to grow to ~ 7 km (-15°C). Hence the presence of ice in this system cannot be discounted across its lifecycle, despite no such indications from the Falcon observations. Cloud drop composition was directly measured through cloud water collection using an Axial Cyclone Cloudwater Collector (AC3; Crosbie et al., 2018), which usually resulted in one sample per cloud leg. These samples were analyzed offline for major ions, pH, and elemental composition.

220 Dry aerosol particle size distributions were measured using the combination of a Laser Aerosol Spectrometer (LAS; TSI Model 3340, 100-3000 nm diameter) and Scanning Mobility Particle Sizer (SMPS; TSI Model 3085 DMA, TSI Model 3776 CPC, 3-100 nm diameter) stitched at 100 nm (Sorooshian et al., 2023). The LAS acquired size distributions at 1 s intervals while the SMPS performed 45 s scans. Here we report size distributions as averages over time periods that include several SMPS scans. Condensation particle counters (CPC; TSI Model 3756 and 3772, respectively) provided ultrafine (>3 nm) and fine (>10 nm) total particle concentrations with an additional fine CPC downstream of a thermal denuder at 350°C providing non-volatile particle concentration (>10 nm). A CCN counter (DMT Model 100; Roberts and Nenes, 2005) provided concentrations at 0.37% supersaturation. Two integrating nephelometers provided dried and humidified (< 1 μm) particle scattering at 450, 550 and 700 nm wavelengths (TSI Model 3563). [The CPCs, CCN counter, and nephelometers all provided data at 1 Hz.](#) Non-refractory aerosol mass concentrations (< 1 μm) were measured [at 30s intervals](#) using a high-resolution time-of-flight Aerosol Mass Spectrometer (AMS; Aerodyne Research Inc.).

230 The FCDP was also used for characterization of super-micrometer aerosol during sampling of clear air ( $q_L < 0.001 \text{ g kg}^{-1}$ , no precipitation,  $\text{RH} < 95\%$ ). This provided particle number and volume estimates (i.e., analogous to those described above for the LAS) at ambient conditions extending to larger sizes to aid characterization of coarse aerosol.

The Falcon was also equipped with a forward-facing camera and a downward-facing Heitronics KT-15 Infrared Thermometer used to determine SST.

## 235 2.4 Auxiliary Datasets

### 2.4.1 MERRA-2

Instantaneous (3 hour) three-dimensional meteorological fields from the NASA Modern-Era Retrospective Analysis for Research and Applications Version 2 (MERRA-2; Gelaro et al., 2017; last access February 2, 2023) were used to provide supporting synoptic scale data for the large-scale environment surrounding each case. Large scale winds, temperature, humidity, and geopotential height data are available on interpolated pressure levels at 25 hPa intervals (in the lower troposphere) and  $0.625^\circ \times 0.5^\circ$  grid spacing. Two-dimensional fields (surface pressure, sea level pressure and surface geopotential) are provided on a collocated grid and used to determine the lower boundary (e.g., for adjacent land masses) and extrapolate the 1000 hPa geopotential height when below the surface. Precipitable water (PW) was estimated by trapezoidal integration of:

$$245 \quad PW = \frac{1}{g} \int_0^{p_{sfc}} q_v dp \quad (1)$$

and the horizontal column moisture flux (MF) similarly calculated using:

$$\mathbf{MF} = \frac{1}{g} \int_0^{p_{sfc}} \mathbf{U}_h q_v dp \quad (2)$$

where  $g$  is the gravitational acceleration,  $p$  ( $p_{sfc}$ ) is (surface) pressure,  $q_v$  the water vapor mixing ratio, and  $\mathbf{U}_h$  is the horizontal vector wind. Contributions to the integral below 1000 hPa were included by using the values of the fields at 1000 hPa.

Airmass trajectories were derived from the MERRA-2 horizontal wind fields averaged over a vertical slab between 950 hPa and 800 hPa to reflect the dominant low-level horizontal motion. The airmass trajectory was solved numerically by integrating the slab wind forward and backwards in time using a linear interpolation of the wind field to the trajectory location and time within the 3-hourly reanalysis outputs. This method of calculating trajectories intentionally ignores reanalysis vertical motion because the main purpose of the trajectories (in the backward direction) was specifically to assess surface source regions and history. Note that slab winds excluded the 975 and 1000 hPa levels to minimize sensitivity to reanalysis near-surface wind structure.



#### 2.4.2 GOES-East Advanced Baseline Imager

Visible (0.6  $\mu\text{m}$ ) satellite imagery from the Advanced Baseline Imager, onboard the 16<sup>th</sup> Geostationary Operational Environmental Satellites (GOES-East) was accessed through the NASA Langley Satellite Cloud and Radiation Property Retrieval System (SatCORPS; last access January 18, 2023). The high resolution ( $\sim 0.5\text{-}1$  km pixel size) imagery was captured over the duration of each flight and relevant adjacent time periods at 20-minute intervals.

#### 2.4.3 Gridded Sea Surface Temperature

Global daily Group for High Resolution Sea Surface Temperature (GHR SST) gridded data at  $0.01^\circ$  spatial resolution were acquired for each flight (GHR SST Level 4 MUR dataset; last access October 18, 2022). The GHR SST dataset combines night time multi-platform satellite-retrieved products with in situ buoy SST measurements (Chin et al., 2017).

### 3 Synoptic Environment

Backward trajectories (Figure 2a) implied a tropical marine airmass origin (over a time period of 8 days) across all cases originating from the central or western tropical Atlantic and conforming to the expected climatological circulation around the subtropical anticyclone. Based on proximity to the North American continent, the airmass history of Case 3 indicated the potential for contributions from continental pollution sources and indeed trajectories extracted for higher altitudes (above 850 hPa, Figure S1) indicated outflow from the eastern United States. Cases 1-3 were all located along the axis of the Gulf Stream (Figure 2b), while the remaining cases were situated over more spatially uniform surface conditions near Bermuda. Data shown in Figure 2b relate to Case 6, but general SST spatial patterns were broadly consistent amongst the other cases (Figure S2), with the caveat that Case 1, which occurred in September, experienced regionally higher SST consistent with the seasonal cycle. The synoptic meteorological environment was broadly similar across cases and an example of the large scale pattern is shown for Case 6 (Figure 2c,d). The center of the subtropical anticyclone (as diagnosed by sea level pressure) was located to the east and a quasi-stationary frontal boundary was located to the north, marking a region containing deep convection with enhanced PW and MF (Figure 2d). Comparisons with other cases can be found in the Supplement (Figure S3). During the majority of the summertime campaign this frontal boundary was a persistent feature, with its position, strength, and characteristics modulated by transient mid-latitude systems and was often anchored to surface features such as the Gulf Stream or the coastal region of the United States. Across cases, the relative position of these major synoptic features remained broadly consistent with respect to the location of the aircraft sampling such that, for Cases 1-3 (located closer to the continent), the anticyclone was farther west with deep convection and frontal cloud generally found near the coast and onshore.

## 4 Mesoscale cloud organization and environment

### 4.1 Satellite Tracking

Each process study flight module was fixed to a visually selected cloud feature that was used by both aircraft as a reference and defined the center point of the sampling region. ~~S~~By design, satellite imagery taken near the midpoint time of each module indicated regions of enhanced cloudiness and visible cloud aggregation collocated with the sampling region (Figure 3), which was approximately bounded by the area spanned by the dropsondes (yellow dots). Most apparent in Cases 1 and 2 but also observed in Cases 3 and 5 was the prevalence of very small cumulus fields elsewhere in the cloud scene and in the periphery of the enhanced cloud regions together with the emergence of cloud free zones often forming in the immediate surroundings. The position of the Falcon spiral profile (orange cross) was usually in one of these clearings 20-40 km from the cluster centroid. Contours of SST indicate the relative position of the module to the axis of the Gulf Stream in Cases 1-3 and the comparatively homogeneous SST in Cases 4-6. In Cases 1 and 2, cloud sampling occurred above the ridge of maximum SST, while Case 3 sampled the cloud system as it crossed the sharp gradient on its northwest edge ( $0.2 \text{ K km}^{-1}$ ).

The cloud cluster anchoring each flight module was tracked using satellite imagery by calculating the maximum cross-correlation associated with sequential images for a region surrounding the cloud cluster (Nieman et al., 1997). Sequential images were analyzed forward and backwards in time to estimate the lifecycle of the feature and the displacements were fit using least squares regression to create a first order (i.e., linear) prediction of the cloud motion zonal and meridional velocity components over the observed lifetime (Table 1). Satellite animations of the cloud scene evolution viewed in the derived (moving) reference frame of the cloud cluster are included as a video supplement.

The longevity of each trackable feature varied from less than two hours (the truncated Case 5A) to more than eight hours. ~~Cases 1 and 2 exhibited the longest-lived features and the lifecycles genesis and lysis of Cases 1 and 2~~ were less conclusive because Case 2 was subsumed into deep convection and Case 1 likely shared the same fate but was first obscured by an over-running altocumulus deck approximately two hours after the aircraft sampling concluded. The lifecycle of the other cases was more obvious because before and after there were either no clouds or limited/negligible aggregation. In Case 4 (Figure 3d) the image corresponds to the midpoint of the primary module (Case 4A), which encompassed most of the mature lifecycle of this cluster. The secondary module located just to the south (Case 4B) was part of the same mesoscale region and the location of this cloud cluster at the time of the image is shown (marked "x"). Figure 3e shows the image at the midpoint of Case 5B, which became the primary module due to the rapid decay of Case 5A and whose clouds no longer exist at the time of the image.

### 4.2 Thermodynamic Profiles

Mean dropsonde vertical profiles of potential temperature ( $\theta$ ) (Figure 4) show similar vertical structure amongst cases, in line with expectations for the summertime lower and mid troposphere in this region. Using case-specific parcel properties representative of the mixed layer, all contained moderate (marginal) convective available potential energy (CAPE) when

320 implementing a pseudo-adiabatic (reversible) assumption and were associated with minimal convective inhibition (CIN)  
(Table 2), as is typical of tropical oceanic soundings (e.g., Betts, 1982, Xu and Emanuel, 1989). Although stable layers were  
present in some cases, notably Case 1 (Figure 4c), other cases (e.g., Case 5) showed little change in stability with altitude.  
From stability alone, there were no indications from the environment precluding deeper convection from developing and  
indeed, for all cases, satellite imagery indicated deep convective cells within 200-400 km.

325 Mean water vapor mixing ratio ( $q_v$ ) indicated more variability amongst cases particularly in the 2-5 km altitude range, which  
coincided with the region of maximum saturation deficit (e.g., compared to the reference wet adiabat) and PW varied from  
35-48 mm (Table 2). Overall, there was not a clear qualitative relationship between the details of the moisture profile and the  
size and extent of the cloud aggregation, as visualized by satellite (Figure 3); [a conclusion also drawn for organization of  
wintertime Atlantic trade wind cumulus \(George et al., 2021\)](#). For example, Case 5 exhibited the smallest cloud features  
330 with the least overall cloud coverage (Table 2) yet the environment of Case 5B had the highest PW.

#### 4.3 Winds

Wind profiles are shown in Figure 5 as hodographs to visualize the effects of vertical shear of the horizontal wind and the  
winds relative to cluster motion. Relative winds can be visualized by shifting the origin to the cluster motion (square  
335 markers) and cloud layer shear can be represented by the vector from cloud base (down triangle) to top (up triangle). All  
cases indicate that cloud motion was close to the cloud base wind vector (within  $1.3 \text{ m s}^{-1}$  relative vector magnitude), while  
the magnitude of the wind shear between cloud base and top varied from  $1.6 \text{ m s}^{-1}$  (Case 4) to  $7.6 \text{ m s}^{-1}$  (Case 2). In Cases 1,  
2, 5 and 6, the cluster motion was aligned (within  $15^\circ$ ) with the major axis of cloud organization (indicated as a dashed line  
in Figure 5), but only in Case 6 was there an absence of any directional shear such that the cluster motion, the shear vector,  
340 and the major axis were all aligned. Cases 1 and 5 exhibited several near-parallel linear cloud features (“cloud streets”) and  
shared a similar near-perpendicular shear vector across the depth of the cloud and it is notable that pronounced linear  
organization occurred in Case 5 despite both weak mean flow and shear. Shear was almost not existent in Case 4 along with  
only marginal directional organization of cloud features within the module, although there was evidence of cloud banding at  
a larger scale ( $\sim 1000 \text{ km}$ ) along a north-south axis east of the module. Case 3 was the only example where the cloud formed  
345 a pronounced linear ( $\sim 40 \text{ km}$ ) feature that was oriented approximately perpendicular to the cluster motion and the shear  
vector, although satellite imagery also indicated that this was part of a larger ( $\sim 200 \text{ km}$ ) organizational pattern of  
interconnected rings extending along the Gulf Stream axis to the northeast.

## 5 Cloud Properties

### 5.1 Cloud height distributions

350 Frequency distributions of the heights of cloud tops detected by HSRL-2 during the King Air module (Figure 6) indicated  
that in four of the cases (Cases 1-3, 5) a pronounced peak in frequency occurred below 1 km with a near-monotonic decrease

with altitude in the 1-2 km thereafter. Across these four cases, the modal altitudes were 100-200 m above the altitude of the lowest cloud base determined from the low-flying Falcon (Table 2) and reflected the relatively high occurrence of very small cumulus anchored atop the marine sub-cloud mixed layer that prevail in peripheral regions surrounding cloud clusters, despite the apparent emergence of clearings on satellite imagery. [The small optically thin clouds captured by the lidar may be more pervasive than indicated by visible satellite imagery \(Mieslinger et al., 2022\)](#). Mixed layer depths (Table 2) were determined from the altitude of the first maximum in relative humidity of the mean dropsonde profile, which also corresponded to the inflection altitude where mean  $\theta$  ( $q_v$ ) substantially increased (decreased) (Figure 4) and were found to be within 50 m of the lowest cloud base. Across these four cases, the lowest lifting condensation level (LCL) determined from the mean dropsonde data was found 70-140 m above the lowest cloud base and attributable to variability in temperature and humidity, while increases in mixed layer depth and the cloud base correlate with increases in the cloud top modal altitude at a degree slightly higher than proportional (1.2) indicating a minor thickening of the small cloud mode with increasing sub-cloud depth.

In stark contrast, the dominant cloud top modes for Cases 4 and 6 were at 2.9 and 2.5 km, respectively. The vertical distribution of clouds was fundamentally different in these cases and pronounced local maxima in the frequency of cloud tops were observed within multiple altitude ranges, while cloud tops observed below 1 km were less frequent, most notably for Case 4. Undoubtedly, some low-lying clouds may be obscured by laterally spreading cloud aloft, and these cases also generally sustained fewer small cumulus in the surrounding environment, as indicated in Figure 3 and as confirmed by in-flight camera imagery. The observations indicate that regions of enhanced stability do not exert an obvious controlling influence on the distribution of cloud tops, except Case 4. Regions of the column with static stability exceeding  $6 \text{ K km}^{-1}$  (shaded in Figure 6) would tend to inhibit further cloud growth, creating the expectation for more cloud tops to be found within those regions. However, local maxima in cloud top frequency are almost equally located above, below, and within stable layers, while some stable layers result in no apparent influence on the vertical distribution entirely.

The  $0^\circ\text{C}$  altitude (marked in Figure 6) has been attributed to a stability enhancement (e.g., Posselt et al., 2008) but in these six cases there was not a conclusive association between stability and the region close to the  $0^\circ\text{C}$  level; however, Cases 1 and 6 (and marginally Case 4) indicated some partiality for cloud tops at that level. It is worth noting that the clouds detected above 4 km in Case 1 were mostly associated with altocumulus that was not coupled to the convection below, except in one region (confirmed via camera imagery) that was associated with a short-lived deeper convective cell, offset from the Falcon's sampling region. In contrast with apparent influence seen in Case 6, Case 2 did not show any relationship between clouds, stability, and the  $0^\circ\text{C}$  level, while no clouds were observed to reach that level in Cases 3 and 5. The cloud tops observed above 4/3/6 km in Case 2/5/6 were determined to be associated with emergent growth of convective turrets that occurred after the start of the Falcon module and so those altitudes were not sampled in situ. Less cloud was observed at all altitudes during Case 5A compared to 5B in agreement with the initially small size of this cluster at the onset of the module and the subsequent decay. Cloud height distributions can also be visualized using the HSRL-2 backscatter curtain plots, which are included in the Supplement (Figure S4).

## 5.2 Vertical Velocity

Figure 7a shows statistics of the vertical distribution of vertical velocity,  $w$ , measured in situ for each case. Each level leg was truncated to remove maneuvers and high-pass filtered (50 s FFT filter) to remove low-frequency biases/drift and any residual airframe dynamical effects. A  $q_L$ -weighted mean was calculated for  $w$ , which represents a characteristic velocity for the convective transport of condensed water (here  $w_L$  is used to specifically differentiate this quantity). The spread of  $w$ , indicated by the 10-90% range, quantifies the relative magnitude of cloudy updrafts and downdrafts (filtered for cloud,  $q_L > 0.02 \text{ g kg}^{-1}$ ).

Across the cases, maximum updrafts varied between  $1.1 \text{ m s}^{-1}$  (Case 4A) and  $9.9 \text{ m s}^{-1}$  (Case 3), while maximum downdraft magnitudes varied between  $1.1 \text{ m s}^{-1}$  and  $6 \text{ m s}^{-1}$  (the same cases, respectively). Updraft and downdraft extrema were all located within 850 m of the highest in-cloud transect, but because cloud top was dynamically evolving it was challenging to classify this level as a fraction of cloud depth. Transects that encountered stronger updrafts also contained stronger downdrafts, resulting in a correlation coefficient, between updraft and downdraft velocity, of  $-0.77$ . The mean updraft velocity exceeded the mean downdraft by 17% in magnitude.

Positive  $w_L$  occurred in 82% of cloud transects and corresponds to a conventional expectation of strong upward flux of cloud water in the convective core with subsiding motion in diluted (i.e., lower  $q_L$ ) peripheral regions and the immediate cloud-free environment. Negative  $w_L$  occurred predominantly near cloud top in a subset of cases and is believed to be an entirely transient characteristic of individual convective turrets because the source of cloud water is condensation in updrafts. Transient negative  $w_L$  may occur when cloud parcels descend after having overshot neutral buoyancy or because of negative buoyancy generated through homogenization of entrained air. While a descending cloud top interface does not necessarily require negative  $w_L$ , transient negative  $w_L$  is associated with a cyclical collapse of the cloud top and this was observed visually during flight, most prominently in Case 3. Here, the upper extent of the cloud rapidly evaporated and descended approximately 1 km in 5 min, as diagnosed by forward camera imagery, thus implying a cloud top recession velocity of  $\sim 3.3 \text{ ms}^{-1}$ , compared to the observed  $w_L$  of  $-1.6 \text{ ms}^{-1}$  measured during the uppermost transect. Case 5A contained the highest occurrence of negative  $w_L$  and within 15-20 min there was no visual evidence of the cloud system, which was confirmed by visible satellite imagery. These cases are too limited in number to provide a statistical description of the behavior of an ensemble of cloudy thermals within a typical system but the occurrence of transient negative  $w_L$  here may be amplified as a consequence of the flight strategy. Emergent convective turrets that were used to anchor the sampling were identified with a lead time of several minutes, so there was a greater chance (than typical) that a selected turret would subsequently be in decline by the time sampling of the cloud top region was underway. Evidence of thermal bubbles exists in the vertical structure of  $w_L$  particularly for Case 3 and the upper half of Case 6. Regions where  $w_L$  was close to zero also tended to occur in parallel with local reductions in the strength of updrafts and downdrafts at that level and are attributed to wake regions detrained from active thermals. While residual turbulence remained in these regions, parcels may be closer to neutral buoyancy representing the more aged regions between rising bubbles or regions where cloud had spread laterally. Beyond

420 the scale of single transects and individual thermals, Case 4A (which was sampled immediately after deeper convection had  
ceased) exemplifies this at the cloud system scale with minimal  $w_L$  and weaker updrafts and downdrafts, in agreement with  
the observed lack of surface-coupled convection and a more stratiform appearance.

### 5.3 Liquid Water Content

425 Vertical gradients of  $q_L$  capture the rate of condensation mediated by the effects of dilution and evaporation from  
entrainment alongside losses due to precipitation. An adiabatic  $q_L$  from a parcel released at the observed lowest cloud base  
for each case (included in Figure 7b) represents an estimate of the  $q_L$  resulting from condensation alone, generally providing  
an upper bound. Near cloud base,  $q_L$  increased with altitude with some cloudy parcels initially approximating the adiabatic  
parcel. With altitude, the envelope of  $q_L$  (as quantified by the upper 90% bound) generally increased at a slower rate (Cases  
430 1, 4B, 5), exhibited little trend (Cases 3, 6), or reverted to a decrease (Case 2). The highest  $q_L$  was observed in Case 3 ( $2.7 \text{ g kg}^{-1}$ )  
despite the fact that the environmental humidity was lowest (Figure 4b). For some upper cloud regions,  $q_L$  tended to  
fluctuate between adjacent sampling levels and this was most notable in Case 6, perhaps accentuated by the cloud system  
depth and the high number of cloud transects. This pattern is indicative of snapshots through an ensemble of transient  
convective elements (e.g., Morrison et al., 2020), where a chain of several rising thermals occurs sequentially, with each  
435 evolving in time, such that the aircraft transects reflect different stages of their lifecycle, proximity to their cores, and  
energetic characteristics. In these dynamic environments, the aircraft measurements cannot singularly isolate vertical  
variability but rather incorporate the temporal evolution of individual thermals and the cloud system at large. Despite  
uncertainty in segregating time evolution and spatial scales of variability, the aircraft snapshot confirms an intermittent  
structure for emergent cores rather than a stationary plume, while at lower altitudes the data are more reflective of the larger  
440 ensemble of contributing thermals at each level.

### 5.4 Cloud droplet number concentration

The overall trend was for droplet number concentration ( $N_d$ ) to decrease with increasing altitude, except Case 5 where a  
minor increase was observed (Figure 7c). In Cases 1 and 3, the trend in  $N_d$  was punctuated by locally anomalous high  
445 concentrations at 2.1 and 3.0 km, respectively, corresponding to local enhancements in the profile of  $q_L$  and were attributable  
to fresh, energetic, convective bubbles. In absence of these singular outliers, Case 1-3 (and Case 6 below 2.5 km) indicated  
near monotonic decreases at a rate of between 27-52%  $\text{km}^{-1}$ . Comparison of the mature/decaying (4A) and active/developing  
(4B) systems of Case 4 showed very close agreement in average  $N_d$  across commonly sampled altitudes, indicating  
robustness in the structure of the profile and suggesting temporal evolution of horizontal mean  $N_d$  may not be substantial  
450 over the system lifecycle [for a congestus complex such as Case 4](#). Cases 4B and 6 exhibited similar vertical patterns with  
decreasing  $N_d$  found below 3 km with subsequent increases to a secondary maximum aloft at 4.3 and 4.6 km, respectively.

The source of  $N_d$  at cloud base is the activation of aerosol particles that serve as cloud condensation nuclei (CCN). The  
number concentration of particles with diameters exceeding 100 nm ( $N_{a,100}$ ) was used as a proxy for the availability of CCN,

455 qualitatively captured the variability in  $N_d$  amongst the cases. The  $N_d$  for Case 5A (decaying) was 45% lower than Case 5B (active) but coincided with a 22% decrease in the below-cloud  $N_{a,100}$ . The fact that the change in  $N_d$  was proportionally greater than the change in aerosol may be explained partly by weaker cloud forming convective updrafts in Case 5A, even though the sub-cloud turbulence was found to be similar (Table 2). The contrasting  $N_d$  behaviour seen in Case 5 compared to the consistent  $N_d$  characteristics of Case 4 highlight the different role of aerosol interactions across lifecycle for different cloud system types. Crucially, a greater desiccation by entrainment because of its smaller size and lack of fresh convection was likely controlling the statistics of  $N_d$  observed in Case 5A. In an attempt to separate initial activation (a topic that will be discussed further in Section 7) from subsequent in-cloud controls on  $N_d$  variability, a reference concentration ( $N_{d0}$ ) was calculated from air parcels near cloud base that indicated recent droplet activation (Conant et al., 2004). Here,  $N_{d0}$  (Table 2) was computed as the mean of data points collected in the lowest two cloud transects, limited to updrafts free from precipitation, and with  $q_L$  within 80% of the reference adiabatic parcel representing a best estimate of the initial cloudy state. 460 The  $q_L$  criterion was relaxed to the maximum observed adiabatic ratio when no data above 80% occurred. The lowest  $N_{d0}$  was found for Case 1 ( $144 \text{ mg}^{-1}$ ) and the highest for Case 3 ( $508 \text{ mg}^{-1}$ ).

$N_d$  data were normalized by  $N_{d0}$  and then compared to the ratio of  $q_L$  and the adiabatic water content (Figure 8), representing a comparison between the observations and an idealized adiabatic parcel. Phrased another way, these normalizations are the fraction of drop number and mass concentration retained, compared to an undilute parcel ascent. Mean properties from each transect (Figure 8a) indicate that reductions in  $q_L$  result in proportionally smaller changes in  $N_d$  such that 96% of the transects lie above the 1:1 line. For clarification, a 1:1 relationship would indicate that number and mass are equally affected by dilution and evaporative losses, suggesting either extreme inhomogeneous mixing or partial volumes of cloudy and clear air at the scale of the measurement ( $\sim 100 \text{ m}$ ). There is no strong divergence or separation in the behavior between cases indicating some degree of universality: the combined data exhibit a positive correlation coefficient ( $R=0.73$ ), and a total least squares linear regression indicates a slope of 1.89. The joint frequency of 1 s cloudy data (rather than transect means) across all cases (Figure 8b) confirms the same enhancement of  $N_d$  over a 1:1 relationship and, for the lower range of  $q_L$  that comprises the majority of the data, suggests that a linear model is appropriate, noting that logarithmically spaced bins were used to better reflect the distribution of data points. At higher  $q_L$ , the use of 1s data shows that the distribution asymptotes towards  $N_{d0}$ , in line with expectations for data to ~~terminate~~ ~~at~~ ~~see~~ around (1,1), by design. Although data points that are 475 close to adiabatic represent a small set of the total observations, separation by vertical velocity (Figure 8c) indicates that this region of the joint histogram is more influenced by updrafts. 480

All else held constant, droplet collisions would reduce  $N_d$  without changing  $q_L$ , while loss of  $q_L$  by accretion of falling precipitation would have a near equivalent impact on  $N_d$ , notwithstanding a strong size dependence of collection efficiency. Therefore, the results shown in Figure 8 indicate that collisions cannot be dominant in shaping the budget and vertical 485 distribution of  $N_d$ , particularly for updrafts.

## 5.5 Drop Size Distributions

Formatted: Subscript

Formatted: Subscript

Anomaly drop size distributions (DSD) were derived from the mean DSD from each cloud leg, normalized by leg mean  $N_d$ , and then compared as a ratio to the normalized mean of all cloud legs (Figure 9). The resulting anomaly DSD vertical profile represents relative enhancements or reductions in the DSD shape compared to the reference DSD shape, without conflating changes in  $N_d$ . The advantage of this approach is that anomalies can be assessed independent of the drastic change in number concentration that occurs over the entire DSD (i.e., both cloud and rain water modes). At each level, the DSD exhibits the combined influence of net condensation, entrainment and subsequent mixing of environmental air, secondary droplet activation, collisions amongst cloud droplets and the removal of drops by falling precipitation. A monodisperse reference drop diameter was calculated using  $N_{d0}$  and  $q_{L,ad}$  to represent idealized behaviour of a reference adiabatic parcel and is overlaid on Figure 9.

We observe three major modes that vary in their degree of significance amongst cases: (i) a condensation/evaporation mode that resembles a “J” shape and closely, but not identically, aligns with the reference monodisperse diameter and could represent upward or downward motion, (ii) a precipitation growth mode that when coupled with the upper section of the “J” forms an inverted “V” and reflects rain drop growth caused by accretion, and (iii) a secondary activation mode that occurs to the left of the “J” and may occur at multiple altitudes.

Positive anomalies associated with mode (i) often track close to the monodisperse adiabatic diameter even with the sub-adiabatic profile of  $q_L$  (Figure 7b) and more importantly, despite the proportional enhancement of  $N_d$  (Figure 8). Extreme inhomogeneous mixing of entrained environmental air would tend to affect  $N_d$  and  $q_L$  equally by completely evaporating a subset of drops while the remaining drops retain their size (Jensen and Baker, 1989). Conversely, homogeneous mixing reduces the size of all drops and, in isolation, could offer a partial explanation for the behaviour shown in Figure 8 where drops lose cloud water or do not grow as fast (reduced  $q_L/q_{L,ad}$ ), but with a lesser impact on  $N_d$  (less reduced  $N_d/N_{d0}$ ). However, the near adiabatic growth of mode (i) (Figure 9) would contradict the assertion; instead indicating that a subset of droplets was shielded from the influence of entrainment. The majority of 1 s observations ([sampling interval](#)) show that  $q_L$  remains distinctly sub-adiabatic, even at the 90% level (Figure 7b), suggesting that any regions of undiluted growth manifest predominantly at scales  $<100$  m ([sampling interval times flight speed](#)).

Mode (i) is often accompanied by additional smaller drops (i.e., explaining the enhanced  $N_d$  behaviour of Figure 8) that sometimes are concentrated at specific sizes (i.e., as mode iii). In addition, the reference normalized DSD in Figure 9 shows pronounced multimodal characteristics that would not be as distinct if it were only representing the averaged growth with altitude of a single broadened mode. While some contributions to mode (iii) may result from mixing that is effectively homogeneous at the smallest scales but inhomogeneous at larger scales (but still  $<100$  m), the magnitudes of the enhancements in mode (iii) are suggestive of episodic, distinct, secondary droplet activation (i.e., events that take place above the lowest cloud base).

The broadening of the DSD with altitude, implied by Figure 9 through the emergence of modes (i) and (iii), was investigated quantitatively using the relative dispersion,  $\epsilon$ , which relates the standard deviation of drop sizes comprising the DSD to the mean size (Tas et al., 2015). As a number-based measure of DSD broadening, the magnitude of  $\epsilon$  is insensitive to the tail of



DSD and therefore not directly impacted by processes relating to precipitation (i.e., the role of mode (ii)). Amongst cases,  $\epsilon$  exhibited similar values (Figure 10) showing a consistent increase with altitude ( $0.075 \text{ km}^{-1}$ ). Across the data, the average  $\epsilon$  was  $0.47 \pm 0.12$ , which is higher than reported for cumulus over land (Tas et al., 2015), potentially because their cases were shallower and more polluted. Furthermore, the updraft dynamics of daytime cloud-forming thermals over land may result in fundamentally different entrainment-microphysics interactions compared to these marine cases. In summary, significant DSD broadening is attributed to entrainment processes; specifically, the combination of inhomogeneous or incomplete mixing of rising parcels together with activation of additional droplets within the time that mixing is taking place.

In all cases there was evidence of precipitation initiation/formation near cloud top, attributed to an active collision/coalescence process causing growth of the anomaly DSD well beyond the adiabatic diameter (Figure 9). However, the emergence of subsequent precipitation growth (mode ii) was most prominent in Cases 2, 4B, and 6, though each case exhibited a marked decrease in the significance of this mode at lower levels. Part of the decrease of the rain mode was attributed to the higher fractional contribution of non-precipitating clouds that did not extend beyond lower altitudes (Figure 6), but it is notable that some cases (3, 4A) exhibited distinct breaks in the precipitation growth mode and may represent the temporal and spatial intermittency of convective transport.

A hypothesis for the rapid decrease in the precipitation mode at lower levels (seen most prominently in Case 3) is that time needed to produce precipitation and enact sufficient growth is in direct competition with the buoyancy “clock” of cloudy volumes, which are progressively succumbing to the effects of continual entrainment and turbulent mixing. Older cloudy volumes that contain nascent precipitation carry a risk that fresh convective bubbles, that carry a buoyancy premium, rise through their midst, expel them laterally, and promote their evaporation into the environment rather than continuing to accrete cloud water. Figure 11 shows four sequential transects from Case 3 between 2-3 km altitude and covering the region where the rain mode appears active in Figure 9. The Falcon position has been projected onto a cloud centric coordinate system using the fitted cloud motion (Table 1) to adjust for drift and rotated such that the x-axis corresponds to the direction of cloud motion. In each leg, a dominant updraft was collocated with a region of high  $q_L$  defining the convective core with adjacent cloudy downdrafts. Rainwater fraction (RWF) was calculated as the fraction of  $q_L$  contributed from drop sizes exceeding  $100 \mu\text{m}$  indicating that while the core was rain free (very low RWF), the downdraft regions at the edge of cloud featured high RWF. This was most prominent for transect #4 at 2.7 km altitude, where high RWF downdrafts were observed on both the entry and exit from cloud in regions with moderate  $q_L$ , such that RWF enhancement in downdrafts cannot be explained by evaporation of small drops alone.

A further aspect of the measurements of droplet microphysics was the availability of remote sensing retrievals to provide additional context as well as performance evaluation. Detailed analysis of the performance of combined HSRL-RSP microphysical retrievals is the topic of further study, and these cases provide unique datasets for that effort. We limit this evaluation to the retrievals of effective radius ( $r_{\text{eff}}$ ) from RSP (note the use of radius here, by convention, while diameter is used everywhere else), which is provided at  $\sim 1.2 \text{ Hz}$  and was combined with the median HSRL-2 cloud height within each period. Statistics were determined for each case by separating the HSRL-2 cloud heights into eight equally sized subsets

from which the mean and 10-90% range of RSP  $r_{\text{eff}}$  were calculated (Figure 12) and compared to the same statistics for each cloudy transect sampled in situ by the Falcon. RSP tended to underestimate the effective radius profile in cases where there was a dominant rain mode; this was clearly captured for Case 6 where there was a closer agreement with in situ data if rain water contributions to  $r_{\text{eff}}$  were omitted. There are two contributing aspects: (i) a lack of sensitivity to rain-sized drops by  
560 RSP (Alexandrov et al., 2018) that can low bias the  $r_{\text{eff}}$  for these cloud systems when RWF is high near cloud top and, (ii) the lack of an optical signature, at RSP wavelengths, of the deep interior of the cloud where most rain-producing drop interactions occur. Unlike the Falcon transects, which provide a statistical representation at each level (notwithstanding biases introduced from transient cloud behaviour), the RSP statistics reflect the microphysics of the outer “crust” of the cloud cluster.

565

### 5.6 Sub-cloud precipitation

Rain rates were determined during in situ sampling legs carried out below cloud base to estimate the significance of surface precipitation. In the absence of radar data, it is challenging to place the under-sampled aircraft data into a statistical context, therefore the reported precipitation reflects only a snapshot and may contain biases associated with the flight strategy. The  
570 upper size limit of the 2D-S (1.5 mm) also under-sizes the contribution from large rain drops, which may cause a low bias in calculated rain rates. Considering these caveats, evaluation of sub-cloud precipitation was more focused on the relative differences between cases than assessing the broader relevance of rain rate absolute values.

Maximum (90%) and mean rain intensities (Table 2) were calculated from DSD data for each sub-cloud altitude using a threshold precipitation rate exceeding 0.01 mm hr<sup>-1</sup> to define rainy regions. The spatial distribution of precipitation tended to  
575 be highly concentrated in visually identifiable rain shafts and the flight line was adjusted to fly through their (visual) center, where possible. In cases where multiple sub-cloud altitudes were flown, the leg with the highest rain coverage and rain intensity was retained. No sub-cloud precipitation was encountered during Case 1 and 5A and in Cases 5B and 3, the rain was concentrated in a single narrow region less than 1 km in horizontal extent. To the extent that was possible, camera imagery was used to confirm that no major region of precipitation was missed simply by the choice of flight track. Case 5B  
580 was unusual because the maximum rain intensity was comparatively high (3.87 mm hr<sup>-1</sup>) but it was limited to a very narrow region (0.6 km) in an otherwise completely non-precipitating cloud line. Conclusions drawn from comparing the maximum or mean rain intensity were similar and, as a singular metric for identifying the significance of precipitation in each case, the mean rain intensity did not capture the extent of the rainy region and therefore would over emphasize precipitation in Cases 3 and 5. Conversely, the transect mean (not included) was heavily biased to the sampling details of each particular case (e. g.  
585 the time spent sampling the clear-sky region). With a desire to derive a characteristic rain rate comparable amongst cases, the fractional rain coverage was estimated as the ratio between (linear distance) rain coverage below cloud and the maximum horizontal linear extent of Falcon cloud sampling aloft at any altitude. The product of the fractional rain coverage and mean rain intensity provided a cluster rain rate (Table 2). While an area fraction would be a more desirable quantity by which to derive this measure, the aircraft sampling tended to align with a principal cloud axis and therefore provided limited

590 information by which to assess a second spatial dimension, and any assumptions would need to be case specific. Using the  
derived cluster rain rate, cases ranged from non-precipitating (1, 5A) to a maximum for Case 4, which interestingly revealed  
similar rates for 4A (0.45 mm hr<sup>-1</sup>) and 4B (0.52 mm hr<sup>-1</sup>) despite their differing convective characteristics, maturity, and  
600 peak rain intensities.

## 6 Composition

### 595 6.1 Trace Gases

In situ bulk statistics (Table 2) and vertical profiles (Figure 13) of CO, CO<sub>2</sub>, CH<sub>4</sub> and O<sub>3</sub> were derived for each case.  
Vertical profiles were separated into data collected during cloud penetrations (in-cloud), adjacent cloud free regions sampled  
between each cloud level (near field), legs below cloud base (sub-cloud) and the spiral profile (far field). Differences  
600 between the near and far field data reflect the influence of the cloud system on the vertical structure of the environment in  
combination with pre-existing horizontal gradients. Differences between the in-cloud and near field data are caused by  
convective transport. For CO, the statistical significance of profile differences was reduced because the magnitudes of the  
CO variations were proportionally smaller compared to the instrument precision (5 ppb<sub>v</sub>, 0.4 Hz).

Near and far field profiles were generally similar across cases except for Case 3. Near field CH<sub>4</sub> and O<sub>3</sub> most closely tracked  
trends associated with the far field vertical structure but tended to filter smaller scale features, perhaps indicating the  
605 influence of convective mixing on the near field environment. This was generally more noticeable in the case of CO<sub>2</sub> where  
far field overall vertical gradients were less apparent. In Case 3, the far field profile was characterized by a significant  
vertical gradient at 1.8-2.0 km where CO, CH<sub>4</sub>, and O<sub>3</sub> rapidly increased (45, 50, 35 ppb<sub>v</sub>, respectively), while CO<sub>2</sub>  
decreased (4 ppm<sub>v</sub>). Above this altitude, O<sub>3</sub> continued to increase while the trend in other species reversed. This pattern was  
610 a result of an airmass of marine origin undercutting a continental airmass aloft that had the signatures of anthropogenic  
influence coupled with a reduced CO<sub>2</sub> background caused by summertime biogenic uptake. The location of Case 3 on the  
gradient between polluted and background airmasses meant that the near field and in cloud concentrations were affected by  
both vertical and horizontal mixing.

In-cloud concentrations generally exhibited a smaller dynamic range, in line with expectations that cumulus serve to  
transport sub-cloud air upwards and vertically homogenize near field environmental air through entrainment and hence their  
615 concentrations reflected a weighted average of sub-cloud and near field properties. In most cases there were many  
combinations of “weights” that could explain the in-cloud concentrations, but in some cases it is possible to do so while  
restricting contributions to the same level and below. Such scenarios are necessary for the archetypal rising entraining plume  
model of cumulus, such that in-cloud concentrations lag vertical gradients in the environment. However, there were  
identifiable cases where the in-cloud concentrations led the environmental gradient, such as O<sub>3</sub> and CH<sub>4</sub> in Case 3 and CO<sub>2</sub>  
620 in Case 2 and (marginally) Case 6. These cases required air from higher altitudes to explain the in-cloud concentrations and  
hence suggests that simplified descriptions of lateral entrainment in shallow cumulus (e.g., de Rooy et al., 2013) should also

account for (i) laterally entraining cloudy downdrafts, which were ubiquitous in all these cases (Figure 7), and (ii) the temporal characteristic of thermal bubbles. Further development and testing of theory and models for cumulus entrainment and detrainment is not the focus here, but these case studies provide comprehensive datasets on which to base such an effort.

625

## 6.2 Aerosols

Aerosol optical property typing provided by HSRL-2 (Burton et al., 2014) indicated the fractional contribution of aerosol types (classified as marine, polluted marine, urban, smoke, fresh smoke, dust, dusty mix) by altitude during the entire King Air module (Figure 14a). The “unclassified” type represents mixes or a lack of typable signatures, while the remaining absent fraction was not typable because of a lack of aerosol scattering, obscuration by cloud, or missing lidar data. A primary signature of marine aerosols was observed for Cases 1-3 with a secondary contribution from continental sources, typed mostly as smoke, influencing layers between 1-2.5 km (particularly in Case 3). Cases 5 and 6 indicated a dominant dust layer, with the influence of marine aerosols taking a secondary role confined to the lowest 500 m. The dust was assumed to be of Saharan origin based on back trajectories and persisted during other ACTIVATE flights during this time period (i.e., flights that were not process studies). [Long-range transport of Saharan dust has been shown to inhibit cloud growth in this region \(Gutleben et al., 2019\) and may partially explain some of the characteristics here \(e.g., the differences between Case 5A and Case 5B\).](#) The smoke classification, and particularly the identification of fresh smoke, during Case 4 was inconsistent and difficult to reconcile because of the absence of candidate sources and other signatures that are expected for smoke such as elevated sub-micrometer organic aerosol mass (Figure 14c) and CO (Figure 13a). The back trajectory and the consistent synoptic pattern across the five days that included Cases 4-6 would create an expectation for Case 4 to share the dust classification of Cases 5 and 6, and indeed aerosols were typed as dusty mix during part of the statistical survey flight in the morning of June 10 (not shown). Both dust and smoke are depolarizing, and it is possible that a misclassification could result from a dusty mix that is more aged, perhaps more coated with secondary aerosol, and contains a higher (optical) influence from accumulation mode particles (of any source) that decreases the particle depolarization and increases the lidar ratio.

630

640

645

Aerosol extinction from HSRL was mostly confined to the lowest 2 km of the atmosphere (Figure 14b), with Cases 1-3 indicating a more prominent enhancement in the lowest 1 km. With a deeper marine mixed layer than other cases, Case 2 exhibited the characteristic signature of aerosol hygroscopic growth leading to a defined maximum in extinction near the top of the mixed layer; a pattern also seen in Case 1 and 3 but associated with a layer that was shallower. In situ sub-micrometer dry extinction was computed from the sum of particle absorption and nephelometer total scattering measured at two relative humidity (RH) levels and was scaled to RH=20 % using a gamma hygroscopic growth model. The contribution from sub-micrometer aerosol water was estimated by determining the sub-micrometer extinction at the ambient RH and subtracting the dry component. The super-micrometer extinction was estimated from particle area derived from the FCDP particle size distribution (assumed to represent ambient RH) and an extinction efficiency calculated from Mie Theory assuming a refractive index for water ( $1.33 \pm 0i$ ). Overall, the in situ components of the ambient extinction capture the shape of the HSRL

650

655

profile but the HSRL profile is generally enhanced in overall magnitude by between 21% (Case 6) and 77% (Case 3). In Cases 1-3, aerosol water contributed between 36% and 47% of the dry extinction to the total sub-micrometer budget within the lowest 1 km, which spanned the mixed layer and the lowest part of the layer occupied by cumulus. It is expected that water would contribute a similar, or larger, component of the super-micrometer extinction for these cases, based on the expectation of sea spray dominance. Both in situ and HSRL data were screened to remove clouds, but both respective methods have unavoidable differences. In addition, the relationship between aerosol water and humidity between 90% and saturation is strongly convex meaning that contributions from air parcels near saturation have a highly disproportionate role and could easily explain the differences seen at low altitude in Cases 1-3. Aerosol water contributed minimally to sub-micrometer extinction in Cases 4-6, consistent with the expectation of dust. The super-micrometer extinction estimates are likely to be more uncertain in these cases because (a) the sizing obtained from the FCDP was derived from an assumption of spherical water droplets, and (b) particles between 1  $\mu\text{m}$  dry diameter and the smallest observable FCDP diameter at ambient humidity would be under-reported.

Non-refractory sub-micrometer particle composition (Figure 14c) was dominated by sulfate in all cases, except Case 3 where some layers were more organic dominant in alignment with a greater influence of continental pollution. While the organic contribution for other cases was too small to further interrogate the characteristics, the Case 3 organic aerosol indicated a lower degree of oxidation, as quantified by the  $f_{44}$  AMS mass fraction, in the region below 1 km (0.10) compared to the 1.5-2.5 km range (0.15). The mass ratio of ammonium to sulfate did not have an observable vertical change and ranged from 0.12-0.27, with Case 1 and 2 less neutralized than ammonium bisulfate, Case 3 approximately equal to ammonium bisulfate and Cases 4-6 lying between bisulfate and fully neutralized ammonium sulfate.

### 6.3 Cloud drop composition

Cloud water composition (Figure 14d) was strongly influenced by sea salt, assumed to be a direct consequence of cumulus clouds lofting air from the marine mixed layer below cloud base and in broad agreement with other recent cloud water measurements of vertically developed cumulus (Crosbie et al., 2022; Stahl et al., 2021). The largest component of cloud water ionic mass can be attributed to sea salt in Cases 1-3 at all altitudes (89-94%, 49-67% and 51-66%, respectively) and is also in support of the increased prevalence of HSRL marine aerosol types below cloud (Figure 14a). The emergence of nitrate in the cloud water composition of Cases 2 and 3 (24-31% and 12-27%, respectively) occurs with an increase in the polluted marine designation by HSRL, perhaps confirming additional influence of anthropogenic sources compared with Case 1. Non sea salt sulfate (4-8%) and organic ions (1-9%) were proportionally enhanced during Case 3, also supporting continental pollution influence. Non-sea salt calcium, a common tracer for dust, was more enhanced in Cases 4-6 (0.9-9%) than 1-3 (0-2%), and, interestingly, this was also accompanied by an increase in non-sea salt potassium in the middle and upper regions particularly for Case 6 and contributed up to 20% by mass. Dust contains a greater fraction of insoluble material which does not contribute to the analysis of cloud water ions. Case 4 and Case 6 also exhibit larger vertical changes in the cloud water composition and that is notable because these cases were deepest and most affected by precipitation,

690 potentially providing a mechanism for increased vertical stratification in drop composition. Enhanced sea salt in energetic cumulus tops has been observed elsewhere (e.g., Crosbie et al., 2022) and featured here mainly in Cases 2, 4B and 6. Notably though, clean regions at higher altitudes and the influence of precipitation removal on solutes may partly explain enhanced variability in relative composition, as small perturbations can generate large influences. Nonetheless, consistency across several sequential data points adds to the robustness of the observed trends.

## 695 **7 CCN Activation and aerosol microphysics**

### **7.1 Sub-cloud Aerosol**

In situ aerosol particle size distributions were compiled for the sub-cloud environment in each case and normalized to unit integral (Figure 15a), showing the merged contributions from the SMPS and LAS. Across all cases the distributions reveal a clear multimodal structure with dominant contributions from Aitken and accumulation modes, separated by well-defined  
700 minima (Hoppel et al., 1986), except Case 3 where the Aitken mode is broader and slightly larger. The less pronounced Hoppel minimum found in Case 3 is aligned with expectations for enhanced influence from continental pollution (see [Section 6](#)), which may have undergone proportionally less cloud processing.

Contributions to each mode are fit to log-normal distributions and parameters are provided in Table 2. Across cases, the Aitken mode varied from 43 to 64 nm, while the accumulation mode varied from 180 to 230 nm. An activation diameter was estimated as the size above which the integrated number concentration would equal the estimated  $N_0$  (Table 2) and ranges from 52 to 74 nm. CCN counter data at 0.37% supersaturation are included in Table 2, but closure of these data to the particle size distributions would require unrealistically high particle hygroscopicity for Cases 4-6 based on equilibrium drop activation calculations (not shown). In lieu of a detailed droplet closure analysis, the LAS number concentration ( $>100$  nm),  $N_{100}$ , is quite effective at predicting  $N_{d0}$  using a constant scaling factor of 1.84, and explains 80% of the variance in  $N_{d0}$   
710 amongst these cases.

### **7.2 Vertical profiles**

Total particle number concentration data are block averaged in altitude bins of 500 m across all cloud free regions to capture the vertical structure of the environment as sampled in situ by the Falcon. Figure 15 (panels b and c) shows the profile of  
715 total particle number concentration ( $>3$  nm,  $N_3$ ), and  $N_{100}$ , as well as their ratio (panel d) and the non-volatile fraction, NVF ( $>10$  nm, panel e).

$N_3$  generally decreased or remained constant through the lowest 2 km and then increased above 3 km. This upward trend is most apparent for the three cases conducted in 2022 from Bermuda (Cases 4-6) where a marked transition to higher concentrations was observed and was also observed to occur for larger particles ( $>100$  nm). In Cases 4 and 6, increasing  $N_3$   
720 with altitude above 3 km was correlated with enhancements in CO and CH<sub>4</sub> (Figure 13) and minor increases in particle organic mass (Figure 14c), suggesting continental origin. While the beginnings of the uptick in particle concentrations were

consistent for Case 5, correlations were not discernible because the vertical extent of the sampling was truncated in line with the vertical extent of the cloud cluster. The close vertical alignment of the increase in  $N_3$  and  $N_{100}$  in the environment (Figure 15) with the inflection in the profile of  $N_d$  for Cases 4B and 6 (Figure 7c) is perhaps an additional indication of secondary activation of entrained CCN. Case 6 offers a favorable dataset to evaluate entrained activation (e.g., in parcel models and LES) because of the sharpness of the aerosol gradient and the abundance of larger ( $N_{100}$ ) particles aloft. In contrast, Cases 2 and 3 show markedly reduced  $N_{100}$  above 3 km, with a major distinction between these two cases occurring between 2-3 km as a result of the organic-rich pollution layer affecting Case 3.

Across all cases the fraction of larger particles decreases with altitude (Figure 15d) with the ratio  $N_{100} / N_3$  varying from 22-40% in the lowest altitude bin to less than 6% above 4 km (for the cases where data was available). NVF provides an indicator for refractory cores enhanced in layers enriched in primary combustion particles as well as dust and sea spray, while low values typically indicate an abundance of (nucleated) secondary aerosol species. At low altitudes, the marine dominated Cases 1 and 2 had the lowest NVF (32% and 42%, respectively) and is supportive of a large number fraction of marine particles originating from new particle formation and subsequent secondary aerosol growth, with the pollution-influenced Case 3 the highest (54%), and the Bermuda 2022 Cases 4-6 tightly clustered between 48% and 50%. Near 2 km, the influence of the continental pollution is most significant in Case 3, as determined by the organic enrichment (Figure 14c), and is accompanied by higher NVF, while Case 2 relaxes to an unperturbed free tropospheric background with low aerosol mass, smaller particles and the lowest NVF. It is notable that in the purportedly dust-influenced layer at 1.5-2.5 km influencing Cases 4-6, there is a distinct difference in NVF between Case 4 (which mimics the enhancements of Case 3) and Cases 5 and 6 (which instead decrease) and may provide further insight into the optical signature leading to the smoke classification of Case 4 (Figure 13a).

## 8 Discussion and Conclusions

This measurement report describes six case studies relating to airborne observations of aggregated regions of marine shallow cumulus and cumulus congestus. The observations incorporate a coordinated flight strategy centered on a target cloud cluster and involved a HU-25 Falcon that sampled the cloud and surrounding environment in situ, while a King Air made repeated remote sensing passes above the scene, dropping dropsondes around the perimeter and near the center.

The large-scale meteorology was broadly consistent across cases, with a subtropical anticyclone located to the east resulting in northward advection of moist tropical airmasses and the PBL airmass origin (8 day) was the trade wind region of the central tropical Atlantic. As the low-level airmasses advected around the southwest quadrant of the subtropical high moving northward into the sub-tropical region, mid-tropospheric temperatures decreased, while SSTs remained close to tropical levels, typical of the summertime western Atlantic. Three of the cases were conducted over the warm Gulf Stream waters near the United States east coast, while the other three occurred over relative uniform SST near Bermuda. The warm, moist advection and surface fluxes maintained the PBL thermodynamic properties close to tropical conditions, while the reduction

in mid-tropospheric temperature may explain the destabilization of the profile, permitting nearby deeper convection, and the  
755 lack of a defined capping inversion for most of the cases.

Overall, there was not a strong association between localized increases in static stability and the frequency of cloud top  
observations at that altitude. This may indicate that the environmental moisture profile, wind shear, cloud horizontal scale,  
and perhaps microphysics all contribute to the vertical distribution of cloud heights in situations where a strong capping layer  
is absent. Also notable was a lack of a universal relationship amongst the cluster motion vector, the shear vector and the  
760 principal linear axis of organization and is perhaps indicative of a memory effect that sustains a favored orientation after  
formation.

Multiple passes through the cloud clusters revealed considerable variability in the cloud system properties compared to an  
idealized adiabatic parcel and confirmed the ubiquity of environmental entrainment in affecting the bulk characteristics.  
Evidence of transient thermals was observed through the variability in the spatial distribution of vertical velocity, bulk water  
765 content and microphysical properties between sequential transects. Downdrafts were commonly observed, often near cloud  
edges, and there were some, albeit limited, examples where gas tracer concentrations within the cloud could only be  
explained by incorporating environmental air from a higher altitude. In some cases, cyclical collapse of emergent convective  
turrets resulted in net downward transport of cloud water near cloud top. These cases offer a unique dataset to evaluate and  
improve convective parameterization of entrainment and detrainment for shallow cumulus.

770 The effect of entrainment on generating sub-adiabatic  $q_L$  was less impactful on  $N_d$  and was found to be generally consistent  
across cases. This was not associated with a uniformly reduced droplet growth rate (as might be anticipated with  
homogeneous mixing), but rather a source of  $N_d$  from activation of entrained air and manifested as a distinct mode of small  
droplets in the DSD occurring alongside a mode that grew close to the (monodisperse) adiabatic rate. The result was a  
broadening of the DSD with altitude, as quantified by the relative dispersion. Further analysis and parcel modeling are  
775 needed to fully explore this concept in detail, but an underpinning factor is that the timescale for entrained air (e.g., at the  
eddy scale of thermals) to homogenize within a cloudy volume is slow compared to the time taken for the entrained air to be  
carried upwards to its particular LCL. Further evidence that pointed towards the activation of entrained air was found in two  
cases where  $N_d$  transitioned to an increase with altitude above 3 km in concert with an increase in the number of CCN-active  
particles in the environment.

780 Precipitation below cloud base was spatially concentrated into narrow regions and in some cases absent or negligible. It was  
found in at least one case that rain water formed near cloud top was expelled laterally by subsequent thermals, where it was  
anticipated that much of the rain water would ultimately evaporate into the dry surrounding environment, explaining the  
limited extent of precipitation at lower altitudes. The cases which exhibited the highest near surface precipitation were  
associated with markedly different frequency distributions of cloud top altitude, perhaps indicating a threshold above which  
785 the precipitation substantially influences the cloud dynamics. The remaining cases would tend to indicate that precipitation  
is a consequence, and not a cause, of aggregation and deepening.



Across the cases, shared attributes may provide useful means to isolate specific mechanisms or modes for further investigation. These are summarized as follows:

- Cases 1 and 5 were the least vertically developed and both exhibited pronounced linear organization with either very isolated or no observed precipitation below cloud base. Cloud motion was slightly ( $8^\circ$  and  $15^\circ$ , respectively) to the left of the axis of cloud organization with veering of the wind (i.e., clockwise rotation) with altitude such that the cloud top to base shear vector was approximately perpendicular to the cloud axis and remarkably similar in magnitude. Different features for Case 1 included steering winds being stronger by a factor of  $\sim 2$ , being located over the Gulf Stream (rather than near Bermuda), and the aerosol was indicative of background marine conditions, while Case 5 was influenced by Saharan dust. Case 5 incorporated observations of two systems: 5A which was decaying and 5B which was active, with 5A more influenced by the Saharan dust.
- Cases 2 and 3 exhibited intermediate levels of vertical development with a clear distinction between the vertically developed cluster and the surrounding boundary layer cumulus and both showed evidence of clearings forming in the immediate surroundings (more notable for Case 2). Both cases were located over the Gulf Stream. Case 3 was more influenced by continental pollution leading to higher  $N_d$ . Convective vertical velocity extrema were stronger in Case 3, perhaps indicating a liquid-phase microphysical invigoration mechanism, while precipitation was more influential for Case 2. A notable difference in the organization was in the orientation of the cloud axis which was parallel to the cluster motion in Case 2 and perpendicular in Case 3.
- Cases 4 and 6 were cumulus congestus cases and the most vertically developed. The vertical distribution of cloud cover was different from the other cases, with the emergence of detrained layers in the environment surrounding the convection. These cases also captured a distinct lifecycle, with the cloud cluster apparently deepening too rapidly to sustain itself. This was captured in the measurements of Case 4A, which sampled the remnants of a previously deeper system and in Case 6, where the cloud system ceased to exist shortly after the sampling was completed. These cases offer unique datasets for detailed analysis of convective lifecycle of cloud clusters.

In conclusion, this measurement report documents a novel strategy of utilizing two coordinated aircraft to conduct in situ and remote sensing observations of aggregated shallow cumulus and cumulus congestus during the NASA EVS-3 ACTIVATE summer field campaigns spanning 2020-2022. Six process study cases have been reported, providing the background and supporting information associated with the measurements to guide further analysis and modeling. [The datasets collected during ACTIVATE provide a unique and comprehensive characterization of dynamic, thermodynamic, trace gas, aerosol and cloud properties at high temporal resolution, and the implementation of this flight strategy provides targeted observations of individual cloud clusters and their environments.](#)

### **Data Availability**

All datasets are publicly available and can be found at <https://doi.org/10.5067/SUBORBITAL/ACTIVATE/DATA001> (NASA/LaRC/ASDC, 2021).

### 820 **Video Supplement**

Satellite animations showing each case study on a cloud-centric moving coordinate system can be found at [https://doi.org/10.5067/ASDC/SUBORBITAL/ACTIVATE-Satellite\\_1](https://doi.org/10.5067/ASDC/SUBORBITAL/ACTIVATE-Satellite_1) (NASA/LaRC/ASDC, 2021).

### **Author Contribution**

825 EC, LDZ, MAS, TS, JWH, AS, RAF designed and implemented the flight strategy. All authors contributed to experimental data collection and EC, LDZ and MAS conducted data analysis. EC led the preparation of the manuscript with contributions from all authors.

### **Competing Interests**

At least one of the authors is a member of the editorial board of Atmospheric Chemistry and Physics.

### **Acknowledgements**

830 We acknowledge the contributions from the pilots and aircraft support personnel from the NASA Langley Research Services Directorate for the successful execution of ACTIVATE flights. This work was supported by ACTIVATE, a NASA Earth Venture Suborbital (EVS-3) investigation funded by NASA's Earth Science Division and managed through the Earth System Science Pathfinder Program Office. CV and SK acknowledge support from the German Research Foundation. [We acknowledge the helpful comments from two anonymous reviewers.](#)

### 835 **Financial Support**

Armin Sorooshian was supported by NASA (grant no. 80NSSC19K0442). Christiane Voigt and Simon Kirschler were funded by the German Research Foundation DFG by SPP 1294 HALO under contract VO 1504/7-1 and VO1504/9-1 and by TRR 301 – Project-ID 428312742.

## References

- 840 Agee, E. M.: Meso-scale cellular convection over the oceans, *Dyn. Atmos. Oceans*, 10, 317–341, 1987.
- Alexandrov, M., Cairns, B., and Mishchenko, M.: Rainbow Fourier transform, *J. Quant. Spectrosc. Ra.*, 113, 2521–2535, <https://doi.org/10.1016/j.jqsrt.2012.03.025>, 2012.
- Alexandrov, M. D., Cairns, B., Sinclair, K., Wasiliewski, A. P., Ziemba, L., Crosbie, E., Moore, R., Hair, J., Scarino, A. J., Hu, Y., Stammes, S., Shook, M. A., and Chen, G.: Retrievals of cloud droplet size from the research scanning polarimeter data: Validation using in situ measurements, *Remote Sens. Environ.*, 210, 76–95, <https://doi.org/10.1016/j.rse.2018.03.005>, 2018.
- 845 Atkinson, B. and Zhang, J.: Mesoscale shallow convection in the atmosphere, *Rev. Geophys.*, 34, 403–431, 1996.
- Baker, M. B., Corbin, R. G., and Latham, J.: The influence of entrainment on the evolution of cloud droplet spectra: I. A model of inhomogeneous mixing, *Q. J. Roy. Meteor. Soc.*, 106, 581–598, <https://doi.org/10.1002/qj.49710644914>, 1980.
- 850 Barrick, J. D. W., Ritter, J. A., Watson, C. E., Wynkoop, M. W., Quinn, J. K. and Norfolk, D. R.: Calibration of NASA turbulent air motion measurement system, NASA Tech. Pap. TP-310, NASA, Washington, D. C., 1996.
- Barthlott, C., Zarbo, A., Matsunobu, T., and Keil, C.: Importance of aerosols and shape of the cloud droplet size distribution for convective clouds and precipitation, *Atmos. Chem. Phys.*, 22, 2153–2172, <https://doi.org/10.5194/acp-22-2153-2022>, 2022.
- 855 Beard, K. V.: Terminal velocity and shape of cloud and precipitation drops aloft, *J. Atmos. Sci.*, 33, 851–864, 1976.
- Berg, L. K., Shrivastava, M., Easter, R. C., Fast, J. D., Chapman, E. G., Liu, Y., and Ferrare, R. A.: A new WRF-Chem treatment for studying regional-scale impacts of cloud processes on aerosol and trace gases in parameterized cumuli, *Geosci. Model Dev.*, 8, 409–429, doi:10.5194/gmd-8-409-2015, 2015.
- 860 Betts, A. K.: Saturation point analysis of moist convective overturning, *J. Atmos. Sci.*, 39, 1484–1505, [https://doi.org/10.1175/1520-0469\(1982\)0392.0.CO;2](https://doi.org/10.1175/1520-0469(1982)0392.0.CO;2), 1982.
- Bony, S., Dufresne, J.-L., Le Treut, H., Morcrette, J.-J., and Senior, C.: On dynamic and thermodynamic components of cloud changes, *Clim. Dynam.*, 22, 71–86, 2004.
- Bony, S. and Dufresne, J.-L.: Marine boundary layer clouds at the heart of tropical cloud feedback uncertainties in climate models, *Geophys. Res. Lett.*, 32, L20806, <https://doi.org/10.1029/2005GL023851>, 2005
- 865 Bony, S., Schulz, H., Vial, J., and Stevens, B.: Sugar, gravel, fish and flowers: Dependence of mesoscale patterns of trade-wind clouds on environmental conditions, *Geophys. Res. Lett.*, 47, e2019GL085988, <https://doi.org/10.1029/2019GL085988>, 2020.
- Bretherton, C., Blossey, P., and Khairoutdinov, M.: An energybalance analysis of deep convective self-aggregation above uniform SST, *J. Atmos. Sci.*, 62, 4273–4292, 2005.

- 870 Bretherton, C. S., Blossey, P. N., and Jones, C. R.: Mechanisms of marine low cloud sensitivity to idealized climate perturbations: A single-LES exploration extending the CGILS cases, *J. Adv. Model. Earth Sy.*, 5, 316–337, <https://doi.org/10.1002/jame.20019>, 2013.
- Bretherton, C. S.: Insights into low-latitude cloud feedbacks from high-resolution models, *Philos. T. Roy. Soc. A*, 373, 20140415, <https://doi.org/10.1098/rsta.2014.0415>, 2015.
- 875 Bretherton, C. S. and Blossey, P. N.: Understanding mesoscale aggregation of shallow cumulus convection using largeeddy simulation, *J. Adv. Model. Earth Sy.*, 9, 2798–2821, <https://doi.org/10.1002/2017MS000981>, 2017.
- Brient, F., Schneider, T., Tan, Z., Bony, S., Qu, X., and Hall, A.: Shallowness of tropical low clouds as a predictor of climate models' response to warming, *Clim. Dynam.*, 433–449, doi:10.1007/s00382-015-2846-0, 2015.
- Brient, F. and Bony, S.: Interpretation of the positive low-cloud feedback predicted by a climate model under global  
880 warming, *Clim. Dynam.*, 40, 2415–2431, 2013.
- Burnet, F. and Brenguier, J. L.: Observational study of the entrainment-mixing process in warm convective clouds, *J. Atmos. Sci.*, 64, 1995–2011, 2007.
- Burton, S. P., Ferrare, R. A., Hostetler, C. A., Hair, J. W., Rogers, R. R., Obland, M. D., Butler, C. F., Cook, A. L., Harper, D. B., and Froyd, K. D.: Aerosol classification using airborne High Spectral Resolution Lidar measurements – methodology  
885 and examples, *Atmos. Meas. Tech.*, 5, 73–98, doi:10.5194/amt-5-73-2012, 2012.
- Burton, S.P., Vaughan, M.A., Ferrare, R.A. and Hostetler, C.A.: Separating mixtures of aerosol types in airborne High Spectral Resolution Lidar data. *Atmos. Meas. Tech.*, 7(2), 419-436, 2014.
- Burton, S., Hostetler, C., Cook, A., Hair, J., Seaman, S., Scola, S., Harper, D., Smith, J., Fenn, M., Ferrare, R., Saide, P. E., Chemyakin, E. V., and Müller, D.: Calibration of a high spectral resolution lidar using a Michelson interferometer, with data  
890 examples from ORACLES, *Appl. Optics*, 57, 6061, <https://doi.org/10.1364/AO.57.006061>, 2018.
- Cairns, B., Russell, E. E., LaVeigne, J. D., and Tennant, P. M. W.: Research scanning polarimeter and airborne usage for remote sensing of aerosols, *Proc. SPIE*, 5158, 33–44, 2003.
- Chin, T. M., Vazquez-Cuervo, J., and Armstrong, E. M.: A multi-scale high-resolution analysis of global sea surface temperature, *Remote Sens. Environ.*, 200, 154–169, <https://doi.org/10.1016/j.rse.2017.07.029>, 2017.
- 895 Corr, C. A., Ziemba, L. D., Scheuer, E., Anderson, B. E., Beyersdorf, A. J., Chen, G., Crosbie, E., Moore, R. H., Shook, M., Thornhill, K. L., Winstead, E., Lawson, R. P., Barth, M. C., Schroeder, J. R., Blake, D. R., and Dibb J. E.: Observational evidence for the convective transport of dust over the Central United States, *J. Geophys. Res.-Atmos.*, 121, 1306–1319, <https://doi.org/10.1002/2015JD023789>, 2016.
- Crosbie, E., Brown, M. D., Shook, M., Ziemba, L., Moore, R. H., Shingler, T., Winstead, E., Thornhill, K. L., Robinson, C.,  
900 MacDonald, A. B., Dadashazar, H., Sorooshian, A., Beyersdorf, A., Eugene, A., Collett Jr., J., Straub, D., and Anderson, B.: Development and characterization of a high-efficiency, aircraft-based axial cyclone cloud water collector, *Atmos. Meas. Tech.*, 11, 5025–5048, <https://doi.org/10.5194/amt-11-5025-2018>, 2018.

- Crosbie, E., Ziemba, L. D., Shook, M. A., Robinson, C. E., Winstead, E. L., Thornhill, K. L., Braun, R. A., MacDonald, A. B., Stahl, C., Sorooshian, A., van den Heever, S. C., DiGangi, J. P., Diskin, G. S., Woods, S., Bañaga, P., Brown, M. D., Gallo, F., Hilario, M. R. A., Jordan, C. E., Leung, G. R., Moore, R. H., Sanchez, K. J., Shingler, T. J., and Wiggins, E. B.: Measurement report: Closure analysis of aerosol–cloud composition in tropical maritime warm convection, *Atmos. Chem. Phys.*, 22, 13269–13302, <https://doi.org/10.5194/acp-22-13269-2022>, 2022.
- De Rooy, W. C., Bechtold, P., Froehlich, K., Hohenegger, C., Jonker, H., Mironov, D., Siebesma, A. P., Teixeira, J., and Yano, J.-I.: Entrainment and detrainment in cumulus convection: an overview, *Q. J. Roy. Meteor. Soc.*, 139, 1–19, 2013.
- Denby, L.: Discovering the Importance of Mesoscale Cloud Organization Through Unsupervised Classification, *Geophys. Res. Lett.*, 47, e2019GL085190, <https://doi.org/10.1029/2019GL085190>, 2020
- Derbyshire, S. H., Beau, I., Bechtold, P., Grandpeix, J.-Y., Piriou, J.- M., Redelsperger, J. L., and Soares, P. M. M.: Sensitivity of moist convection to environmental humidity, *Q. J. Roy. Meteorol. Soc.*, 130, 3055–3079, <https://doi.org/10.1256/qj.03.130>, 2004.
- Dickerson, R. R., Huffman, G. J., Luke, W. T., et al.: Thunderstorms: An important mechanism in the transport of air pollutants, *Science*, 235, 460–465, 1987.
- DiGangi, J. P., Choi, Y., Nowak, J. B., Halliday, H. S., Diskin, G. S., Feng, S., Barkley, Z. R., Lauvaux, T., Pal, S., Davis, K. J., Baier, B. C., and Sweeney, C.: Seasonal Variability in Local Carbon Dioxide Biomass Burning Sources Over Central and Eastern US Using Airborne In Situ Enhancement Ratios. *Journal of Geophysical Research: Atmospheres*, 126(24), e2020JD034525. <https://doi.org/10.1029/2020JD034525>, 2021
- Diskin, G. S., Podolske, J. R., Sachse, G. W., and Slate, T. A.: Open-path airborne tunable diode laser hygrometer. *Diode Lasers and Applications in Atmospheric Sensing*, 4817, 196–204. <https://doi.org/10.1117/12.453736>, 2002.
- Fan, J., Rosenfeld, D., Zhang, Y., Giangrande, S. E., Li, Z., Machado, L. A. T., Martin, S. T., Yang, Y., Wang, J., Artaxo, P., Barbosa, H. M. J., Braga, R. C., Comstock, J. M., Feng, Z., Gao, W., Gomes, H. B., Mei, F., Pöhlker, C., Pöhlker, M. L., Pöschl, U., and de Souza, R. A. F.: Substantial convection and precipitation enhancements by ultrafine aerosol particles, *Science*, 359, 411–418, <https://doi.org/10.1126/science.aan8461>, 2018.
- Feingold, G. and Kreidenweis, S. M.: Does cloud processing of aerosol enhance droplet concentrations?, *J. Geophys. Res.*, 105(D19), 24 351–24 361, 2000.
- Flossmann, A., Hall, W., and Pruppacher. H.: A theoretical study of the wet removal of atmospheric pollutants: Part I: The redistribution of aerosol particles capture through nucleation and impaction scavenging by growing cloud drops, *J. Atmos. Sci.*, 42, 583–606, 1985.
- Fried, A., Barth, M., Bela, M., Weibring, P., Richter, D., Walega, J., Li, Y., Pickering, K., Apel, E., Hornbrook, R., Hills, A., Riemer, D. D., Blake, N., Blake, D., Schroeder, J. R., Luo, Z. J., Crawford, J. H., Olson, J., Rutledge, S., Betten, D., Biggerstaff, M. I., Diskin, G., Sachse, G., Campos, T., Flocke, F., Weinheimer, A., Cantrell, C., Pollack, I., Peischl, J., Froyd, K., Wisthaler, A., Mikoviny, T., and Woods, S.: Convective transport of formaldehyde to the upper troposphere and

- lower stratosphere and associated scavenging in thunderstorms over the central United States during the 2012 DC3 study, *J. Geophys. Res.-Atmos.*, 121, 7430–7460, <https://doi.org/10.1002/2015JD024477>, 2016.
- Gelaro, R., McCarty, W., Suárez, M. J., Todling, R., Molod, A., Takacs, L., Randles, C. A., Darmenov, A., Bosilovich, M. G., Reichle, R., Wargan, K., Coy, L., Cullather, R., Draper, C., Akella, S., Buchard, V., Conaty, A., da Silva, A. M., Gu, W., Kim, G.-K., Koster, R., Lucchesi, R., Merkova, D., Nielsen, J. E., Partyka, G., Pawson, S., Putman, W., Rienecker, M., Schubert, S. D., Sienkiewicz, M., and Zhao, B.: The Modern-Era Retrospective Analysis for Research and Applications, Version 2 (MERRA-2), *J. Climate*, 30, 5419–5454, <https://doi.org/10.1175/JCLI-D-16-0758.1>, 2017.
- [George, G., Stevens, B., Bony, S., Klingebiel, M., and Vogel, R.: Observed impact of meso-scale vertical motion on cloudiness, \*J. Atmos. Sci.\*, 78, 2413–2427, <https://doi.org/10.1175/JAS-D-20-0335.1>, 2021.](#)
- 945 George, G., Stevens, B., Bony, S., Vogel, R., and Naumann, A. K.: Widespread shallow mesoscale circulations observed in the trades. *Nat. Geosci.* 16, 584–589. <https://doi.org/10.1038/s41561-023-01215-1>. 2023.
- Goren, T., Kazil, J., Hoffmann, F., Yamaguchi, T., and Feingold, G.: Anthropogenic Air Pollution Delays Marine Stratocumulus Breakup to Open Cells, *Geophys. Res. Lett.*, 46, 14135–14144, <https://doi.org/10.1029/2019GL085412>, 2019.
- 950 Grabowski, W. W. and Morrison, H.: Supersaturation, buoyancy, and deep convection dynamics, *Atmos. Chem. Phys.*, 21, 13997–14018, <https://doi.org/10.5194/acp-21-13997-2021>, 2021.
- Gryspeerd, E., Stier, P., White, B. A., and Kipling, Z.: Wet scavenging limits the detection of aerosol effects on precipitation, *Atmos. Chem. Phys.*, 15, 7557–7570, doi:10.5194/acp-15-7557-2015, 2015.
- [Gutleben, M., Groß, S., and Wirth, M.: Cloud macro-physical properties in Saharan-dust-laden and dust-free North Atlantic trade wind regimes: a lidar case study, \*Atmos. Chem. Phys.\*, 19, 10659–10673, <https://doi.org/10.5194/acp-19-10659-2019>, 2019.](#)
- 955 Hair, J. W., Hostetler, C. A., Cook, A. L., Harper, D. B., Ferrare, R. A., Mack, T. L., Welch, W., Izquierdo, L. R., and Hovis, F. E.: Airborne High Spectral Resolution lidar for profiling aerosol optical properties, *Appl. Opt.*, 47, 6734–6752, 2008.
- Haynes, J. M. and Stephens, G. L.: Tropical oceanic cloudiness and the incidence of precipitation: Early results from CloudSat, *Geophys. Res. Lett.*, L09811, <https://doi.org/10.1029/2007GL029335>, 2007.
- Held, I. M., Hemler, R. S., & Ramaswamy, V.: Radiative-convective equilibrium with explicit two-dimensional moist convection. *J. Atmos. Sci.* 50(23), 3909–3927. 1993.
- Hohenegger, C. and Stevens, B.: Preconditioning deep convection with cumulus convection, *J. Atmos. Sci.*, 70, 448–464, <https://doi.org/10.1175/JAS-D-12-089.1>, 2013.
- 965 Holloway, C. E., Wing, A. A., Bony, S., Muller, C., Masunaga, H., L'Ecuyer, T. S., Turner, D. D., and Zuidema, P.: Observing convective aggregation, *Surv. Geophys.*, 38, 1199–1236, 2017
- Hoppel, W. A., Frick, G. M., and Larson, R. E.: Effect of nonprecipitating clouds on the aerosol size distribution in the marine boundary layer, *Geophys. Res. Lett.*, 13, 125–128, <https://doi.org/10.1029/GL013i002p00125>, 1986.

Hoppel, W. A., Frick, G. M., Fitzgerald, J. W., and Larson, R. E.: Marine Boundary layer measurements of new particle formation and the effects nonprecipitating clouds have on aerosol size distribution, *J. Geophys. Res.*, 99, 14443–14459, 1994.

Igel, A. L. and van den Heever, S. C.: Invigoration or Enervation of Convective Clouds by Aerosols?, *Geophys. Res. Lett.*, 48, e2021GL093804, <https://doi.org/10.1029/2021GL093804>, 2021.

Janssens, M., de Arellano, J. V.-G., Scheffer, M., Antonissen, C., Siebesma, A. P., and Glassmeier, F.: Cloud Patterns in the Trades Have Four Interpretable Dimensions, *Geophys. Res. Lett.*, 48, e2020GL091001, <https://doi.org/10.1029/2020GL091001>, 2021.

Janssens, M., De Arellano, J. V. G., Van Heerwaarden, C. C., De Roode, S. R., Siebesma, A. P., & Glassmeier, F.: Nonprecipitating Shallow Cumulus Convection Is Intrinsically Unstable to Length Scale Growth, *J. Atmos. Sci.*, 80(3), 849–870. 2023.

Jensen, M. P. and Del Genio, A. D.: Factors limiting convective cloud-top height at the ARM Nauru island climate research facility, *J. Climate*, 19, 2105–2117, 2006.

Jensen, J. and Baker, M.: A Simple Model of Droplet Spectral Evolution during Turbulent Mixing., *J. Atmos. Sci.*, 46, 2812–2829, 1989.

Johnson, R. H., Rickenbach, T. M., Rutledge, S. A., Ciesielski, P. E., and Schubert, W. H.: Trimodal Characteristics of Tropical Convection, *J. Climate*, 12, 2397–2418, [https://doi.org/10.1175/1520-0442\(1999\)0122.0.CO;2](https://doi.org/10.1175/1520-0442(1999)0122.0.CO;2), 1999.

Johnson, R. H. and Lin, X.: Episodic Trade Wind Regimes over the Western Pacific Warm Pool, *J. Atmos. Sci.*, 54, 2020–2034, doi:10.1175/1520-0469(1997)0542.0.CO;2, 1997.

Khain, A., Rosenfeld, D., and Pokrovsky, A.: Aerosol impact on the dynamics and microphysics of deep convective clouds, *Q. J. R. Meteorol. Soc.*, 131, 2639–2663, <https://doi.org/10.1256/qj.04.62>, 2005.

Khairoutdinov, M. and Randall, D.: High-resolution simulation of shallow-to-deep convection transition over land, *J. Atmos. Sci.*, 63, 3421–3436, 2006.

Kirschler, S., Voigt, C., Anderson, B., Campos Braga, R., Chen, G., Corral, A. F., Crosbie, E., Dadashazar, H., Ferrare, R. A., Hahn, V., Hendricks, J., Kaufmann, S., Moore, R., Pöhlker, M. L., Robinson, C., Scarino, A. J., Schollmayer, D., Shook, M. A., Thornhill, K. L., Winstead, E., Ziemba, L. D., and Sorooshian, A.: Seasonal updraft speeds change cloud droplet number concentrations in low-level clouds over the western North Atlantic, *Atmos. Chem. Phys.*, 22, 8299–8319, <https://doi.org/10.5194/acp-22-8299-2022>, 2022.

Kirschler, S., Voigt, C., Anderson, B. E., Chen, G., Crosbie, E. C., Ferrare, R. A., Hahn, V., Hair, J. W., Kaufmann, S., Moore, R. H., Painemal, D., Robinson, C. E., Sanchez, K. J., Scarino, A. J., Shingler, T. J., Shook, M. A., Thornhill, K. L., Winstead, E. L., Ziemba, L. D., and Sorooshian, A.: Overview and statistical analysis of boundary layer clouds and precipitation over the western North Atlantic Ocean, *Atmos. Chem. Phys.*, 23, 10731–10750, <https://doi.org/10.5194/acp-23-10731-2023>, 2023.

- Koch, D., Park, J., and Del Genio, A.: Clouds and sulfate are anticorrelated: A new diagnostic for global sulfur models, *J. Geophys. Res.*, 108, 4781, doi:10.1029/2003JD003621, 2003.
- Koren, I., Kaufman, Y., Rosenfeld, D., Remer, L., and Rudich, Y.: Aerosol invigoration and restructuring of Atlantic convective clouds, *Geophys. Res. Lett.*, 32, L14828, doi:10.1029/2005GL023187, 2005.
- 1005 Koren, I., Martins, J. V., Remer, L. A., and Afargan, H.: Smoke invigoration versus inhibition of clouds over the Amazon, *Science*, 321, 946, doi:10.1126/science.1159185, 2008.
- Koren, I., Dagan, G., and Altaratz, O.: From aerosol-limited to invigoration of warm convective clouds, *Science*, 344, 1143–1146, 2014.
- 1010 Kuang, Z. and Bretherton, C. S.: A mass-flux scheme view of high-resolution simulation of a transition from shallow to deep cumulus convection, *J. Atmos. Sci.*, 63, 1895–1909, 2006.
- Kumar, B., Götzfried, P., Suresh, N., Schumacher, J., and Shaw, R. A.: Scale dependence of cloud microphysical response to turbulent entrainment and mixing, *J. Adv. Model. Earth Sy.*, 10, 2777–2785, 2018.
- 1015 Lawson, R. P., O'Connor, D., Zmarzly, P., Weaver, K., Baker, B., Mo, Q., and Jonsson, H.: The 2D-S (stereo) probe: Design and preliminary tests of a new airborne, high-speed, high-resolution particle imaging probe, *J. Atmos. Ocean. Techn.*, 23, 1462–1477, 2006.
- LeMone, M. A. and Meitin, R. J.: Three examples of fair weather mesoscale boundary-layer convection in the tropics, *Mon. Weather Rev.*, 112, 1985–1997, 1984.
- Li, Y., Pickering, K. E., Barth, M. C., Bela, M. M., Cummings, K. A., and Allen, D. J.: Evaluation of Parameterized Convective Transport of Trace Gases in Simulation of Storms Observed During the DC3 Field Campaign, *J. Geophys. Res.-Atmos.*, 123, 11238–11261, <https://doi.org/10.1029/2018JD028779>, 2018.
- Leung, G. R. and van den Heever, S. C.: Controls on the Development and Circulation of Terminal versus Transient Congestus Clouds and Implications for Midlevel Aerosol Transport, *J. Atmos. Sci.*, 79, 3083–3101, <https://doi.org/10.1175/JAS-D-21-0314.1>, 2022
- 1025 Luo, Z., Liu, G. Y., Stephens, G. L., and Johnson, R. H.: Terminal versus transient cumulus congestus: A CloudSat perspective, *Geophys. Res. Lett.*, 36, L05808, <https://doi.org/10.1029/2008GL036927>, 2009.
- Malkus, J. and Riehl, H.: Cloud structure and distributions over the tropical pacific ocean, *Tellus*, 16, 275–287, 1964
- Mapes, B. E. and Houze, R. A.: Cloud Clusters and Superclusters over the Oceanic Warm Pool, *Mon. Weather Rev.*, 121, 1398–1415, [https://doi.org/10.1175/1520-0493\(1993\)1212.0.CO;2](https://doi.org/10.1175/1520-0493(1993)1212.0.CO;2), 1993.
- 1030 Marinescu, P. J., van den Heever, S. C., Heikenfeld, M., Barrett, A. I., Barthlott, C., Hoose, C., Fan, J., Fridlind, A. M., Matsui, T., Miltenberger, A. K., Stier, P., Vie, B., White, B. A., and Zhang, Y.: Impacts of Varying Concentrations of Cloud Condensation Nuclei on Deep Convective Cloud Updrafts-A Multimodel Assessment, *J. Atmos. Sci.*, 78, 1147–1172, <https://doi.org/10.1175/JAS-D-20-0200.1>, 2021.
- Masunaga, H.: Free-tropospheric moisture convergence and tropical convective regimes. *Geophys. Res. Lett.*, 41(23), 8611–8618. 2014.
- 1035



Mieslinger, T., Stevens, B., Kölling, T., Brath, M., Wirth, M., and Buehler, S. A.: Optically thin clouds in the trades, *Atmos. Chem. Phys.*, 22, 6879–6898, <https://doi.org/10.5194/acp-22-6879-2022>, 2022.

Mohrmann, J., Bretherton, C. S., McCoy, I. L., McGibbon, J., Wood, R., Ghate, V., Albrecht, B., Sarkar, M., Zuidema, P., and Palikonda, R.: Lagrangian Evolution of the Northeast Pacific Marine Boundary Layer Structure and Cloud during CSET, *Mon. Weather Rev.*, 147, 4681–4700, <https://doi.org/10.1175/MWRD-19-0053.1>, 2019.

Morrison, H., Peters, J. M., Varble, A. C., Hannah, W. M., & Giangrande, S. E.: Thermal chains and entrainment in cumulus updrafts. Part I: Theoretical description. *J. Atmos. Sci.*, 77(11), 3637–3660. 2020.

Muller, C. J. and Held, I. M.: Detailed Investigation of the SelfAggregation of Convection in Cloud-Resolving Simulations, *J. Atmos. Sci.*, 69, 2551–2565, 2012.

NASA/LaRC/SD/ASDC: Aerosol Cloud meTeorology Interactions oVer the western ATlantic Experiment, NASA Langley Atmospheric Science Data Center DAAC [data set], <https://doi.org/10.5067/SUBORBITAL/ACTIVATE/DATA001>. 2021.

Narenpitak, P., Kazil, J., Yamaguchi, T., Quinn, P., and Feingold, G.: From sugar to flowers: A transition of shallow cumulus organization during ATOMIC, *J. Adv. Model. Earth Sy.*, 13, e2021MS002619, <https://doi.org/10.1029/2021MS002619>, 2021.

Nesbitt, S. W., Cifelli, R., and Rutledge, S. A.: Storm morphology and rainfall characteristics of TRMM precipitation features, *Mon. Weather Rev.*, 134, 2702–2721, <https://doi.org/10.1175/MWR3200.1>, 2006.

Nieman, S. J., Menzel, W. P., Hayden, C. M., Gray, D., Wanzong, S. T., Velden, C. S., and Daniels, J.: Fully automatic cloud drift winds in NESDIS operations, *B. Am. Meteorol. Soc.*, 78, 1121– 1133, 1997.

Nuijens, L., Serikov, I., Hirsch, L., Lonitz, K., and Stevens, B.: The distribution and variability of low-level cloud in the North Atlantic trades, *Q. J. Roy. Meteor. Soc.*, 140, 2364–2374, <https://doi.org/10.1002/qj.2307>, 2014.

Posselt, D. J., van den Heever, S. C., and Stephens, G. L.: Trimodal cloudiness and tropical stable layers in simulations of radiative convective equilibrium, *Geophys. Res. Lett.*, 35, L08802, <https://doi.org/10.1029/2007GL033029>, 2008.

Rangno, A. L. and Hobbs, P. V.: Microstructures and precipitation development in cumulus and small cumulonimbus clouds over the warm pool of the tropical Pacific Ocean, *Q. J. Roy. Meteor. Soc.*, 131, 639–673, <https://doi.org/10.1256/qj.04.13>, 2005.

Rauber, R. M., Stevens, B., Ochs, III, H. T., Knight, C., Albrecht, B. A., Blyth, A. M., Fairall, C. W., Jensen, J. B., Lasher-Trapp, S. G., Mayol-Bracero, O. L., Vali, G., Anderson, J. R., Baker, B. A., Bandy, A. R., Burnet, E., Brenguier, J. L., Brewer, W. A., Brown, P. R. A., Chuang, P., Cotton, W. R., Girolamo, L. D., Geerts, B., Gerber, H., Goke, S., Gomes, L., Heikes, B. G., Hudson, J. G., Kollias, P., Lawson, R. P., Krueger, S. K., Lenschow, D. H., Nuijens, L., O’Sullivan, D. W., Rilling, R. A., Rogers, D. C., Siebesma, A. P., Snodgrass, E., Stith, J. L., Thornton, D. C., Tucker, S., Twohy, C. H., and Zuidema, P.: Rain in shallow cumulus over the ocean – The RICO campaign, *B. Am. Meteorol. Soc.*, 88, 1912–1928, [doi:10.1175/BAMS-88-12-1912](https://doi.org/10.1175/BAMS-88-12-1912), 2007.

- Redelsperger, J.-L., Parsons, D. B., and Guichard, F.: Recovery Processes and Factors Limiting Cloud-Top Height following the Arrival of a Dry Intrusion Observed during TOGA COARE, *J. Atmos. Sci.*, 59, 2438–2457, [https://doi.org/10.1175/1520-0469\(2002\)0592.0.co;2](https://doi.org/10.1175/1520-0469(2002)0592.0.co;2), 2002.
- 1070 Reid, J. S., Posselt, D. J., Kaku, K., Holz, R. A., Chen, G., Eloranta, E. W., Kuehn, R. E., Woods, S., Zhang, J., Anderson, B., Bui, T. P., Diskin, G. S., Minnis, P., Newchurch, M. J., Tanelli, S., Trepte, C. R., Thornhill, K. L., and Ziemba, L. D.: Observations and hypotheses related to low to middle free tropospheric aerosol, water vapor and altocumulus cloud layers within convective weather regimes: a SEAC4RS case study, *Atmos. Chem. Phys.*, 19, 11413–11442, <https://doi.org/10.5194/acp-19-11413-2019>, 2019.
- 1075 Rieck, M., Nuijens, L., and Stevens, B.: Marine Boundary Layer Cloud Feedbacks in a Constant Relative Humidity Atmosphere, *J. Atmos. Sci.*, 69, 2538–2550, 2012.
- Riehl, H. and Malkus, J. S.: On the heat balance in the equatorial trough zone, *Geophysica*, 6, 503–558, 1958.
- Roberts, G. C. and Nenes, A.: A Continuous-Flow Streamwise Thermal-Gradient CCN Chamber for Atmospheric  
1080 Measurements, *Aerosol Sci. Technol.*, 39, 206–221, doi:10.1080/027868290913988, 2005.
- Romps, D. M. and Kuang, Z.: Do undiluted convective plumes exist in the upper tropical troposphere?, *J. Atmos. Sci.*, 67, 468–484, doi:10.1175/2009JAS3184.1, 2010.
- Rosenfeld, D., Lohmann, U., Raga, G. B., O’Dowd, C. D., Kulmala, M., Fuzzi, S., Reissell, A., and Andreae, M. O.: Flood or drought: How do aerosols affect precipitation?, *Science*, 321, 1309–1313, <https://doi.org/10.1126/science.1160606>, 2008.
- 1085 Rosenfeld, D. and Lensky, I. M.: Satellite-based insights into precipitation formation processes in continental and maritime convective clouds, *Bull. Amer. Meteorol. Soc.*, 79, 2457–2476, 1998.
- Rowe, A. K. and Houze Jr., R. A.: Cloud organization and growth during the transition from suppressed to active MJO conditions, *J. Geophys. Res.-Atmos.*, 120, 10324–10350, <https://doi.org/10.1002/2014JD022948>, 2015.
- Ruppert, J. H., & Johnson, R. H.: Diurnally modulated cumulus moistening in the preonset stage of the Madden–Julian oscillation during DYNAMO. *J. Atmos. Sci.*, 72(4), 1622–1647. 2015.
- 1090 Schulz, H., Eastman, R., and Stevens, B.: Characterization and Evolution of Organized Shallow Convection in the Downstream North Atlantic Trades, *J. Geophys. Res.-Atmos.*, 126, e2021JD034575, <https://doi.org/10.1029/2021JD034575>, 2021.
- Seifert, A. and Heus, T.: Large-eddy simulation of organized precipitating trade wind cumulus clouds, *Atmos. Chem. Phys.*,  
1095 13, 5631–5645, <https://doi.org/10.5194/acp-13-5631-2013>, 2013.
- Semie, A. G., and Bony, S.: Relationship between precipitation extremes and convective organization inferred from satellite observations. *Geophysical Research Letters*, 47(9), e2019GL086927. 2020.
- Sherwood, S. C., Bony, S., and Dufresne, J. L.: Spread in model climate sensitivity traced to atmospheric convective mixing, *Nature*, 505, 37–42, 2014.
- 1100 Snodgrass, E. R., Di Girolamo, L., and Rauber, R. M.: Precipitation Characteristics of Trade Wind Clouds during RICO Derived from Radar, Satellite, and Aircraft Measurements, *J. Appl. Met.*, 48, 464–483, 2009.

Sobel, A. H. and Bretherton, C. S.: Modeling tropical precipitation in a single column, *J. Climate*, 13, 4378–4392, 2000.

Sokolowsky, G. A., Freeman, S. W., and van den Heever, S. C.: Sensitivities of Maritime Tropical Trimodal Convection to Aerosols and Boundary Layer Static Stability, *J. Atmos. Sci.*, 79, 2549– 2570, <https://doi.org/10.1175/JAS-D-21-0260.1>,  
1105 2022.

Sorooshian, A., Anderson, B., Bauer, S. E., Braun, R. A., Cairns, B., Crosbie, E., Dadashazar, H., Diskin, G., Ferrare, R., Flagan, R. C., Hair, J., Hostetler, C., Jonsson, H. H., Kleb, M. M., Liu, H. Y., MacDonald, A. B., McComiskey, A., Moore, R., Painemal, D., Russell, L. M., Seinfeld, J. H., Shook, M., Smith, W. L., Thornhill, K., Tselioudis, G., Wang, H. L., Zeng, X. B., Zhang, B., Ziemba, L., and Zuidema, P.: Aerosol-Cloud Meteorology Interaction Airborne Field Investigations: Using  
1110 Lessons Learned from the US West Coast in the Design of ACTIVATE off the US East Coast, *B. Am. Meteorol. Soc.*, 100, 1511– 1528, <https://doi.org/10.1175/Bams-D-18-0100.1>, 2019.

Sorooshian, A., Alexandrov, M. D., Bell, A. D., Bennett, R., Betito, G., Burton, S. P., Buzanowicz, M. E., Cairns, B., Chemyakin, E. V., Chen, G., Choi, Y., Collister, B. L., Cook, A. L., Corral, A. F., Crosbie, E. C., van Dienenhoven, B., DiGangi, J. P., Diskin, G. S., Dmitrovic, S., Edwards, E.-L., Fenn, M. A., Ferrare, R. A., van Gilst, D., Hair, J. W., Harper,  
1115 D. B., Hilario, M. R. A., Hostetler, C. A., Jester, N., Jones, M., Kirschler, S., Kleb, M. M., Kusterer, J. M., Leavor, S., Lee, J. W., Liu, H., McCauley, K., Moore, R. H., Nied, J., Notari, A., Nowak, J. B., Painemal, D., Phillips, K. E., Robinson, C. E., Scarino, A. J., Schlosser, J. S., Seaman, S. T., Seethala, C., Shingler, T. J., Shook, M. A., Sinclair, K. A., Smith Jr., W. L., Spangenberg, D. A., Stammes, S. A., Thornhill, K. L., Voigt, C., Vömel, H., Wasilewski, A. P., Wang, H., Winstead, E. L., Zeider, K., Zeng, X., Zhang, B., Ziemba, L. D., and Zuidema, P.: Spatially coordinated airborne data and complementary  
1120 products for aerosol, gas, cloud, and meteorological studies: the NASA ACTIVATE dataset , *Earth Syst. Sci. Data*, 15, 3419–3472, <https://doi.org/10.5194/essd-15-3419-2023>, 2023.

Stahl, C., Crosbie, E., Bañaga, P. A., Betito, G., Braun, R. A., Cainglet, Z. M., Cambaliza, M. O., Cruz, M. T., Dado, J. M., Hilario, M. R. A., Leung, G. F., MacDonald, A. B., Magnaye, A. M., Reid, J., Robinson, C., Shook, M. A., Simpas, J. B., Visaga, S. M., Winstead, E., Ziemba, L., and Sorooshian, A.: Total organic carbon and the contribution from speciated  
1125 organics in cloud water: airborne data analysis from the CAMP2Ex field campaign, *Atmos. Chem. Phys.*, 21, 14109–14129, <https://doi.org/10.5194/acp-21-14109-2021>, 2021.

Stein, T. H. M., Holloway, C. E., Tobin, I., and Bony, S.: Observed relationships between cloud vertical structure and convective aggregation over tropical ocean, *J. Climate*, 30, 2187–2207, <https://doi.org/10.1175/JCLI-D-16-0125.1>, 2017.

Stevens, B., Bony, S., Brogniez, H., Hentgen, L., Hohenegger, C., Kiemle, C., L’Ecuyer, T. S., Naumann, A. K., Schulz, H.,  
1130 Siebesma, P. A., Vial, J., Winker, D. M., and Zuidema, P.: Sugar, gravel, fish and flowers: Mesoscale cloud patterns in the trade winds, *Q. J. Roy. Meteor. Soc.*, 146, 141–152, <https://doi.org/10.1002/qj.3662>, 2020.

Storer, R. L., van den Heever, S. C. and Stephens, G. L.: Modeling Aerosol Impacts on Convective Storms in Different Environments, *J. Atmos. Sci.*, 67, 3904-3915, <https://doi.org/10.1175/2010JAS3363.1>, 2010.

Storer R. L. and Van den Heever, S. C.: Microphysical processes evident in aerosol forcing of tropical deep convective  
1135 clouds, *J. Atmos. Sci.*, 70, 430–446, 2013.

- Takayabu, Y. N., Yokomori, J., and Yoneyama, K.: A diagnostic study on interactions between atmospheric thermodynamic structure and cumulus convection over the tropical western Pacific Ocean and over the Indochina Peninsula., *J. Meteor. Soc. Japan*, 84, 151–169, 2006
- Tao, W.-K., Chen, J.-P., Li, Z., Wang, C., and Zhang, C.: Impact of aerosols on convective clouds and precipitation, *Rev. Geophys.*, 50, RG2001, <https://doi.org/10.1029/2011RG000369>, 2012.
- 1140 Tas, E., Teller, A., Altaratz, O., Axisa, D., Bruintjes, R., Levin, Z., and Koren, I.: The relative dispersion of cloud droplets: its robustness with respect to key cloud properties, *Atmos. Chem. Phys.*, 15, 2009–2017, <https://doi.org/10.5194/acp-15-2009-2015>, 2015.
- Textor, C., Schulz, M., Guibert, S., Kinne, S., Balkanski, Y., Bauer, S., Bernsten, T., Berglen, T., Boucher, O., Chin, M., Dentener, F., Diehl, T., Easter, R., Feichter, H., Fillmore, D., Ghan, S., Ginoux, P., Gong, S., Grini, A., Hendricks, J., Horowitz, L., Huang, P., Isaksen, I., Iversen, I., Kloster, S., Koch, D., Kirkevåg, A., Kristjansson, J. E., Krol, M., Lauer, A., Lamarque, J. F., Liu, X., Montanaro, V., Myhre, G., Penner, J., Pitari, G., Reddy, S., Seland, Ø., Stier, P., Takemura, T., and Tie, X.: Analysis and quantification of the diversities of aerosol life cycles within AeroCom, *Atmos. Chem. Phys.*, 6, 1777–1813, <https://doi.org/10.5194/acp-6-1777-2006>, 2006.
- 1145 Thornhill, K. L., Anderson, B. E., Barrick, J. D. W., Bagwell, D. R., Friesen, R., and Lenschow, D. H.: Air motion intercomparison flights during Transport and Chemical Evolution in the Pacific (TRACE-P)/ACE-ASIA, *J. Geophys. Res.*, 108(D20), 9001, doi:10.1029/2002JD003108, 2003.
- Tobin, I., Bony, S., and Roca, R.: Observational evidence for relationships between the degree of aggregation of deep convection, water vapor, surface fluxes, and radiation, *J. Climate*, 25, 6885–6904, 2012.
- 1155 Tompkins, A.: Organization of tropical convection in low vertical wind shears: The role of cold pools, *J. Atmos. Sci.*, 58, 1650–1672, 2001.
- Tompkins, A. M. and Craig, G.: Radiative-convective equilibrium in a three-dimensional cloud-ensemble model, *Q. J. Roy. Meteorol. Soc.*, 124, 2073–2097, 1998.
- Twomey, S.: The influence of pollution on the shortwave albedo of clouds, *J. Atmos. Sci.*, 34, 1149–1152, [https://doi.org/10.1175/1520-0469\(1977\)0342.0.CO;2](https://doi.org/10.1175/1520-0469(1977)0342.0.CO;2), 1977.
- 1160 Varble, A.: Erroneous Attribution of Deep Convective Invigoration to Aerosol Concentration, *J. Atmos. Sci.*, 75, 1351–1368, <https://doi.org/10.1175/JAS-D-17-0217.1>, 2018.
- Vial, J., Bony, S., Dufresne, J.-L., and Roehrig, R.: Coupling between lower-tropospheric convective mixing and lowlevel clouds: Physical mechanisms and dependence on convection scheme, *J. Adv. Model. Earth Sy.*, 8, 1892–1911, <https://doi.org/10.1002/2016MS000740>, 2016.
- 1165 Vogel, R., Albright, A. L., Vial, J., George, G., Stevens, B., and Bony, S.: Strong cloud-circulation coupling explains weak trade cumulus feedback, *Nature*, 612, 696–700, <https://doi.org/10.1038/s41586-022-05364-y>, 2022.
- Vömel, H., Goodstein, M., Tudor, L., Witte, J., Fuchs-Stone, Ž., Sentic, S., Raymond, D., Martinez-Claros, J., Juracic, A., Maithel, V., and Whitaker, J. W.: High-resolution in situ observations of atmospheric thermodynamics using dropsondes

- 1170 during the Organization of Tropical East Pacific Convection (OTREC) field campaign, *Earth Syst. Sci. Data*, 13, 1107–1117, <https://doi.org/10.5194/essd-13-1107-2021>, 2021.
- Vömel, H., Sorooshian, A., Robinson, C., Shingler, T. J., Thornhill, K. L., and Ziemba, L. D.: Dropsonde observations during the Aerosol Cloud meTeorology Interactions oVer the western ATlantic Experiment, *Scientific Data*, 10, 753, [10.1038/s41597-023-02647-5](https://doi.org/10.1038/s41597-023-02647-5), 2023.
- 1175 Waite, M. L. and Khouider, B.: The deepening of tropical convection by congestus preconditioning, *J. Atmos. Sci.*, 67, 2601–2615, 2010.
- Wang, H., Feingold, G., Wood, R., and Kazil, J.: Modelling microphysical and meteorological controls on precipitation and cloud cellular structures in Southeast Pacific stratocumulus, *Atmos. Chem. Phys.*, 10, 6347–6362, [doi:10.5194/acp-10-6347-2010](https://doi.org/10.5194/acp-10-6347-2010), 2010.
- 1180 Wang, H., Easter, R. C., Zhang, R., Ma, P., Singh, B., Zhang, K., Ganguly, D., Rasch, P. J., Burrows, S. M., Ghan, S. J., Lou, S., Qian, Y., Yang, Y., Feng, Y., Flanner, M., Leung, L. R., Liu, X., Shrivastava, M., Sun, J., Tang, Q., Xie, S., and Yoon, J.: Aerosols in the E3SM Version 1: New Developments and Their Impacts on Radiative Forcing, *J. Adv. Model. Earth Syst.*, 12, 293, 2020.
- Warren, S. G., Hahn, C. J., London, J., Chervine, R. M., and Jenne, R. L.: Global distribution of total cloud cover and cloud  
1185 type amounts over the ocean, NCAR/TN-317 STR, NCAR Tech. Note., 41 pp., 1988.
- Webb, M. J. and Lock, A. P.: Coupling between subtropical cloud feedback and the local hydrological cycle in a climate model, *Clim. Dynam.*, 41, 1923–1939, 2013.
- Williamson, C. J., Kupc, A., Axisa, D., Bilsback, K. R., Bui, T., Campuzano-Jost, P., Dollner, M., Froyd, K. D., Hodshire, A. L., Jimenez, J. L., Kodros, J. K., Luo, G., Murphy, D. M., Nault, B. A., Ray, E. A., Weinzierl, B., Wilson, J. C., Yu, F.,  
1190 Yu, P., Pierce, J. R., and Brock, C. A.: A large source of cloud condensation nuclei from new particle formation in the tropics, *Nature*, 574, 399–403, 2019.
- Wing, A. A. and Emanuel, K. A.: Physical mechanisms controlling self-aggregation of convection in idealized numerical modeling simulations, *J. Adv. Model. Earth Sy.*, 6, 59–74, 2014.
- Wonaschütz, A., Sorooshian, A., Ervens, B., Chuang, P. Y., Feingold, G., Murphy, S. M., de Gouw, J., Warneke, C., and  
1195 Jonsson, H. H.: Aerosol and gas re-distribution by shallow cumulus clouds: an investigation using airborne measurements, *J. Geophys. Res.-Atmos.*, 117, D17202, [doi:10.1029/2012JD018089](https://doi.org/10.1029/2012JD018089), 2012.
- Wood, R., Kuan-Ting, O., Bretherton, C. S., Mohrmann, J., Albrecht, B. A., Zuidema, P., Ghate, V., Schwartz, C., Eloranta, E., Glienke, S., Shaw, R. A., Fugal, J., and Minnis, P.: Ultraclean Layers and Optically Thin Clouds in the Stratocumulusto-Cumulus Transition. Part I: Observations, *J. Atmos. Sci.*, 75, 1631–1652, <https://doi.org/10.1175/JAS-D-17-0213.1>, 2018.
- 1200 Wood, R. and Hartmann, D. L.: Spatial Variability of Liquid Water Path in Marine Low Cloud: The Importance of Mesoscale Cellular Convection, *J. Climate*, 19, 1748–1764, <https://doi.org/10.1175/JCLI3702.1>, 2006.
- Xu, K.-M. and Emanuel, K. A.: Is the Tropical Atmosphere Conditionally Unstable?, *Mon. Weather Rev.*, 117, 1471–1479, [https://doi.org/10.1175/1520-0493\(1989\)1172.0.CO;2](https://doi.org/10.1175/1520-0493(1989)1172.0.CO;2), 1989.

- 1205 Xue, H., Feingold, G., and Stevens, B.: Aerosol effects on clouds, precipitation, and the organization of shallow cumulus convection, *J. Atmos. Sci.*, 65, 392–406, 2008.
- Xue, H. W. and Feingold, G.: Large-eddy simulations of trade wind cumuli: Investigation of aerosol indirect effects, *J. Atmos. Sci.*, 63, 1605–1622, <https://doi.org/10.1175/jas3706.1>, 2006.
- Zuidema, P.: Convective Clouds over the Bay of Bengal, *Mon. Weather Rev.*, 131, 780–798, [https://doi.org/10.1175/1520-0493\(2003\)1312.0.CO;2](https://doi.org/10.1175/1520-0493(2003)1312.0.CO;2), 2003.
- 1210 Zuidema, P., Li, Z., Hill, R. J., Bariteau, L., Rilling, B., Fairall, C., Brewer, W. A., Albrecht, B., and Hare, J.: On Trade Wind Cumulus Cold Pools, *J. Atmos. Sci.*, 69, 258–280, 2012.

Table 1: Cloud cluster sampling characteristics, lifecycle and motion for Cases 1-6.

			1	2	3	4		5		6
			9/29/2020	6/2/2021	6/7/2021	6/10/2022		6/11/2022		6/14/2022
						(A)	(B)	(A)	(B)	
Module Midpoint	Time	(UTC)	15:54	19:00	19:07	19:13	20:11	18:32	19:49	15:05
	Latitude	(°)	37.80	34.41	36.31	31.71	31.17	30.38	31.09	30.45
	Longitude		-70.11	-74.83	-73.60	-65.56	-65.96	-65.54	-64.40	-64.31
Duration	King Air	(hr)	1.2	1.4	1.6	3.3	-	0.8	1.5	2.5
	Falcon		0.8	0.9	1.4	1.7	0.8	0.5	1.5	2.2
Fitted cloud drift velocity	U	$\text{ms}^{-1}$	0.96	-0.78	3.12	5.29	5.40	0.74	1.15	3.98
	V		7.40	7.61	4.32	3.29	2.28	3.76	2.88	3.28
	dU/dt	$\text{ms}^{-1} \text{hr}^{-1}$	0.22	0.52	0.18	-0.16	-0.58	0.51	0.30	1.10
	dV/dt		0.19	0.50	0.64	-0.16	-0.49	-0.45	-0.56	0.34
Lifecycle	Start	(UTC)	12:40	13:40	14:00	16:20	18:00	17:40	17:40	12:20
	End		18:00	21:20	20:40	21:00	21:00	19:00	21:00	16:20
	Lifetime	(hr)	5.3	7.7	6.7	4.7	3	1.3	3.3	4

**Table 2: Cloud and environmental properties of Cases 1-6.**

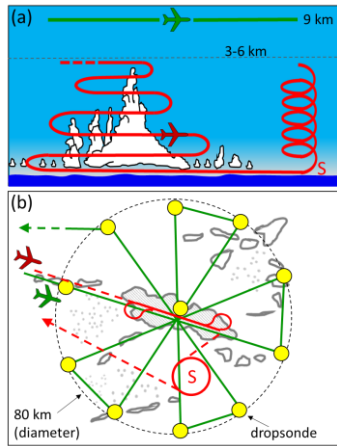
		1	2	3	4		5		6	Source <sup>a</sup>	Notes	
					A	B	A	B				
Cloud Fraction		-	0.47	0.38	0.23	0.42		0.095	0.26	0.33	K	HSRL cloud top detection
Mixed layer height		m	290	490	370	100		290	220	350	D	First max in RH (see text)
Lowest cloud base		m	285	530	413	1100	325	340	225	440	F	Falcon cloud detection and camera
Height of max. cloud top frequency		m	510	790	650	2860	-	460	390	2520	K	HSRL cloud top detection
Sea Level Pressure		hPa	1013.7	1019.8	1019.9	1016.9		1019.4	1019.7	1019.7	D	
Mixed Layer	$\theta$	K	298.3 $\pm 0.3$	296.5 $\pm 0.15$	297.7 $\pm 0.23$	296.3 $\pm 0.18$		297.3 $\pm 0.12$	296.8 $\pm 0.16$	297.6 $\pm 0.09$	D	
	$q_v$	g kg <sup>-1</sup>	17.7 $\pm 0.40$	14.2 $\pm 0.42$	16.3 $\pm 0.35$	17.4 $\pm 0.15$		16.9 $\pm 0.34$	17.1 $\pm 0.23$	16.3 $\pm 0.23$	D	
	U	m s <sup>-1</sup>	0.4 $\pm 0.6$	-2.6 $\pm 0.7$	3.7 $\pm 0.7$	2.5 $\pm 0.6$		0.6 $\pm 0.5$	0.8 $\pm 0.6$	2.5 $\pm 0.6$	D	
	V	m s <sup>-1</sup>	8.1 $\pm 1.4$	7.8 $\pm 0.9$	3.9 $\pm 1.0$	4.8 $\pm 0.8$		3.9 $\pm 0.5$	3.9 $\pm 0.5$	2.5 $\pm 0.9$	D	
	$\sigma_w$	m s <sup>-1</sup>	0.5	0.7	0.6	0.3	1.0	0.5	0.5	0.6	F	Turbulent winds
LWP		g m <sup>-2</sup>	936	1480	2680	629	2340	1410	2650	3360	F	Integrated mean water content
PW		kg m <sup>-2</sup>	45.3	37.7	35.4	47.4		45.7	48.3	41.8	D	Eq 1 applied to mean dropsonde $q_v$
$N_{d,0}$		mg <sup>-1</sup>	144	175	508	315	301	212	302	170	F	adiabatic cloudbase estimate (see text)
CCN 0.37%		mg <sup>-1</sup>	-	197	437	513	481	256	380	193	F	
$N_1$		mg <sup>-1</sup>	179	197	908	412	417	182	258	159	F	Fitted lognormal distribution parameters
$D_1$		nm	43	47	64	55	62	56	64	51	F	
$\sigma_1$		-	0.17	0.18	0.24	0.19	0.19	0.19	0.16	0.18	F	
$N_2$		mg <sup>-1</sup>	86	149	106	187	160	123	135	100	F	
$D_2$		nm	198	186	231	180	189	194	190	179	F	
$\sigma_2$		-	0.16	0.16	0.11	0.15	0.13	0.13	0.09	0.14	F	
$D_{act}$		nm	52	74	69	68	74	57	56	54	F	
AOD		-	0.093	0.064	0.096	0.16		0.14	0.1	0.1	K	HSRL extinction
w [max/min]		m s <sup>-1</sup>	-5.22, 5.29	-2.88, 4.35	-5.70, 10.9	- 1.24, 1.01	- 3.29, 6.83	-3.53, 2.08	-3.88, 5.79	-5.53, 8.39	F	
CAPE	pseudo adiabatic	J kg <sup>-1</sup>	960	228	612	471		757	703	650	D	using mixed layer properties above
	reversible		217	-	33	40		66	51	31	D	
CIN		J kg <sup>-1</sup>	3	3	5	3		3	2	5	D	



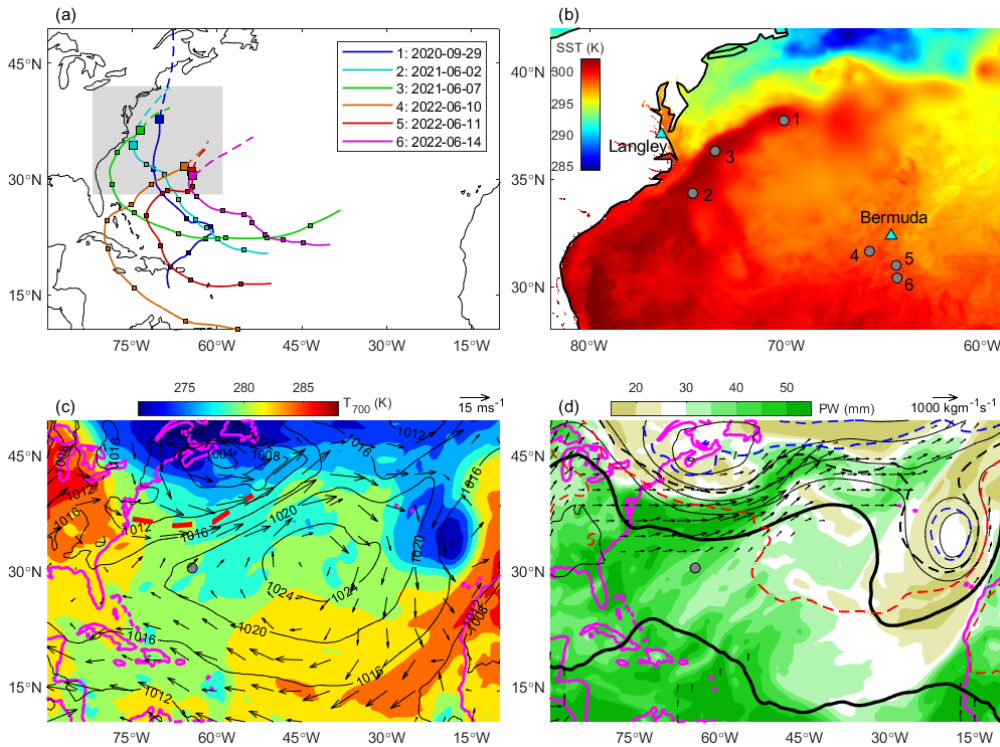
LCL	m	426	639	501	222		410	342	546	D	
SST	K	301.1	299.4	300.9	297.2	297.7	298.9	298.3	300.0	F	KT-15
SHF	W m <sup>-2</sup>	4	-1	2	3	-	-7	-1	-1	F	eddy covariance at minimum altitude
LHF	W m <sup>-2</sup>	159	122	38	24	-	40	18	72	F	eddy covariance at minimum altitude
CO	ppbv	86 ± 4	83 ± 3	90 ± 7	85 ± 3	86 ± 3	80 ± 3	81 ± 5	72 ± 3	F	module average concentration
CO <sub>2</sub>	ppmv	409 ± 0.3	419 ± 0.2	419 ± 0.7	421 ± 0.2	420 ± 0.3	420 ± 0.2	420 ± 0.2	420 ± 0.2	F	
CH <sub>4</sub>	ppbv	1914 ± 4	1908 ± 1	1925 ± 6	1922 ± 4	1925 ± 8	1916 ± 2	1922 ± 12	1918 ± 4	F	
O <sub>3</sub>	ppbv	28 ± 7	28 ± 11	34 ± 17	24 ± 6	31 ± 14	17 ± 4	19 ± 4	23 ± 12	F	
Max Rain Intensity	mm hr <sup>-1</sup>	-	1.55	0.97	2.58	4.29	-	3.87	4.41	F	
Mean Rain Intensity	mm hr <sup>-1</sup>	-	0.47	0.35	0.97	1.41	-	1.11	1.53	F	
Rain coverage	km	-	7.1	0.7	17.1	9.2	-	0.6	10.4	F	
Fractional rain coverage	-	-	0.24	0.02	0.47	0.36	-	0.02	0.17	F	
Cluster Rain Rate	mm hr <sup>-1</sup>	-	0.11	0.007	0.45	0.52	-	0.02	0.26	F	

a Source: K = King Air observations, D = Dropsonde, F = Falcon observations

1220



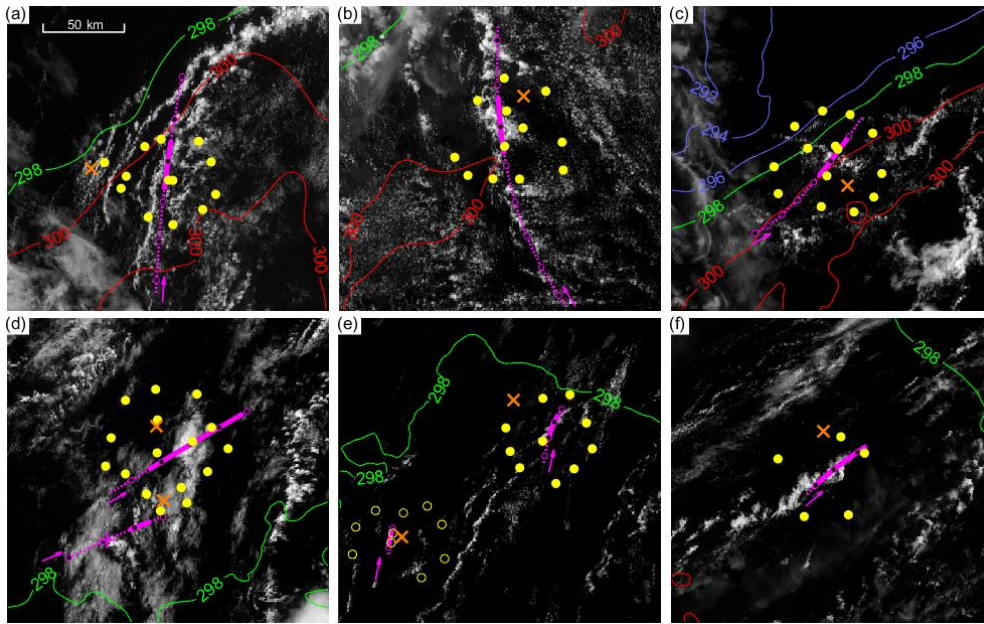
1225 Figure 1: Schematic of the nominal two aircraft flight strategy illustrating the position of the King Air (green) and the Falcon (red): (a) Cross section view of the altitude profile flown through the target cloud with adjacent clear spiral (S), and (b) plan view showing the “wheel and spoke” pattern.



1230

Figure 2: Large-scale meteorological environment. (a) 8-day back trajectory (solid) and 1-day forward trajectory (dashed) using MERRA-2 800-950 hPa layer averaged winds (see text) for Cases 1-6. (b) Example SST shown for Case 6 (2022-06-14) with all case locations shown for reference. The region in (b) corresponds to the grey shaded region of (a). (c) Case 6: sea-level pressure (contours), 850 hPa wind vectors, and 700 hPa temperature (colored). The location of the axis of the stationary front (see text) is shown as the thick red dash. (d) Case 6: 500 hPa geopotential height (contours at 6 dm intervals, thick contour designates the 588 dm level), 1000-500 hPa thickness (dashed contours at 6 dm intervals, black contour designates the 564 dm thickness line, red (blue) contours represent regions of higher (lower) thickness), PW (colored), and MF (vectors).

1235



1240

Figure 3: GOES-East ABI visible ( $0.6 \mu\text{m}$ ) satellite imagery at the midpoint time of each process study: (a)-(f) Case 1-6, respectively, with a scale bar shown in panel (a). Overlaid in each panel: SST (K, contours), dropsonde locations (yellow dots), Falcon clear spiral location (orange cross), cloud cluster track (magenta). The cloud cluster track (see text) is separated into the timeframe of aircraft sampling (solid) and the remaining time window of the cluster lifetime (dotted).

1245

Hourly increments are shown as circles and an adjacent arrow shows the direction of travel. (d) and (e) are images from the midpoint of Case 4A and 5B, respectively. No dropsondes were associated with Case 4B, but its cloud track is shown to the southwest of Case 4A; the location of the tracked Case 4B cluster at the time of the panel (d) image is marked with a plus symbol (+). Dropsondes associated with Case 5A are shown as open circles in panel (e) and the tracked cluster had already dissipated.

1250

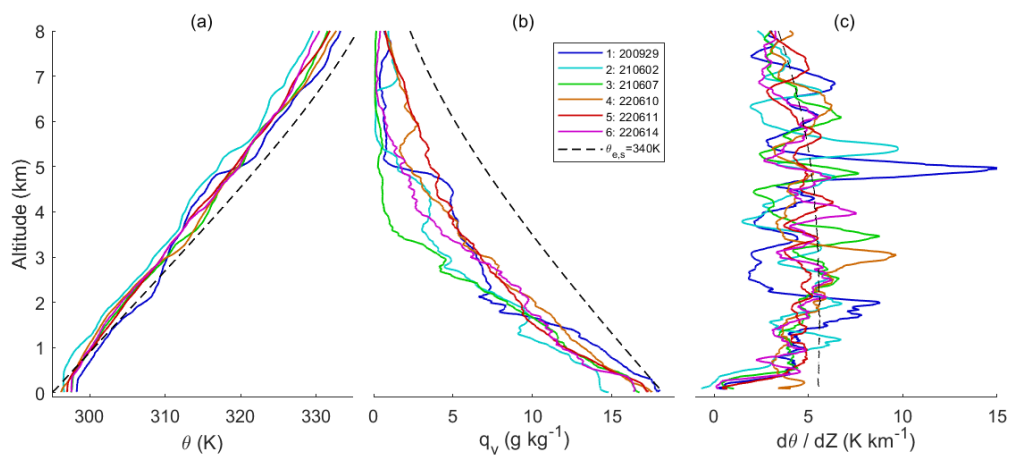


Figure 4: Case-mean dropsonde profiles of (a) potential temperature, (b) water vapor mixing ratio, and (c) static stability (defined as the vertical gradient of potential temperature and smoothed over a 100 m window). The profile of a reference wet adiabat corresponding to a saturation equivalent potential temperature ( $\theta_{e,s}$ ) at 340 K is also shown.

1255

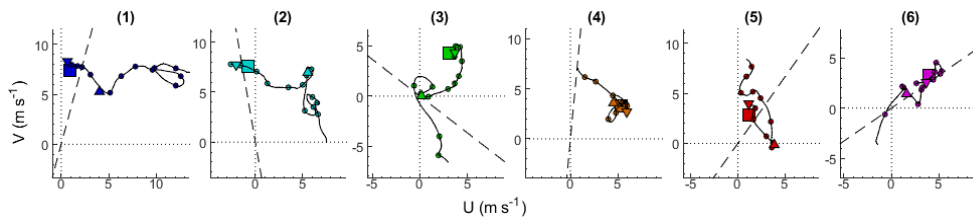
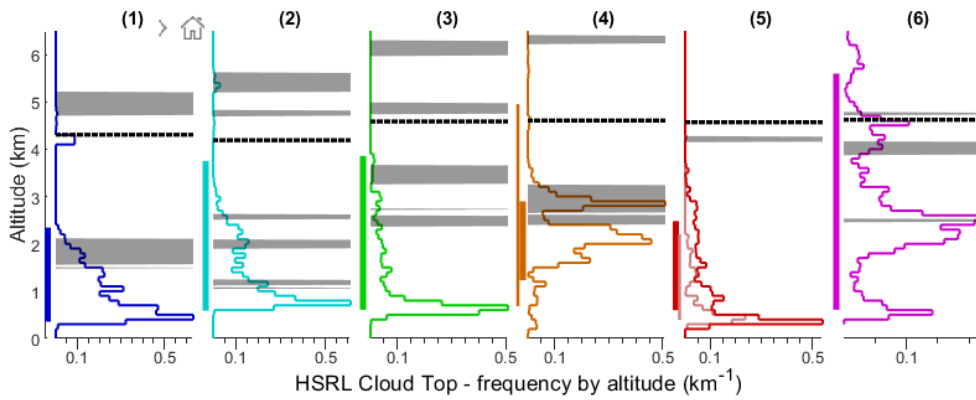


Figure 5: Case-mean dropsonde wind profiles displayed as hodographs for Cases 1-6. The wind profile is smoothed with a 25 hPa running mean and markers (o) indicate increments of 50 hPa. Also included are winds at cloud base (down triangle) and cloud top (up triangle, estimated based on the top of the Falcon module), the mean cluster motion from satellite (square), and the primary principal axis of cloud organization estimated/assessed from satellite (dashed line). In each panel, the scale is preserved with the position of the origin shifted to center the data. Case 5A dropsondes are omitted from (5) for readability but indicate similar structure to Case 5B (shown).

1260



1265

Figure 6: Frequency distributions of HSRL detected cloud tops for Cases 1-6. Frequency data are normalized by the total available records within the module, such that an integration of the distribution results in the HSRL cloud fraction (Table 2). Also shown are regions where  $d\theta/dz$  exceeds  $6 \text{ K km}^{-1}$  as an indicator of stable layers (grey shading), and the  $0^\circ\text{C}$  level (dashed). The vertical bar adjacent to each case indicates the span of altitudes sampled in situ by the Falcon, and in panel (4) and (5), the altitude span for the secondary Falcon modules (thin bar, Cases 4B and 5A, respectively).

1270

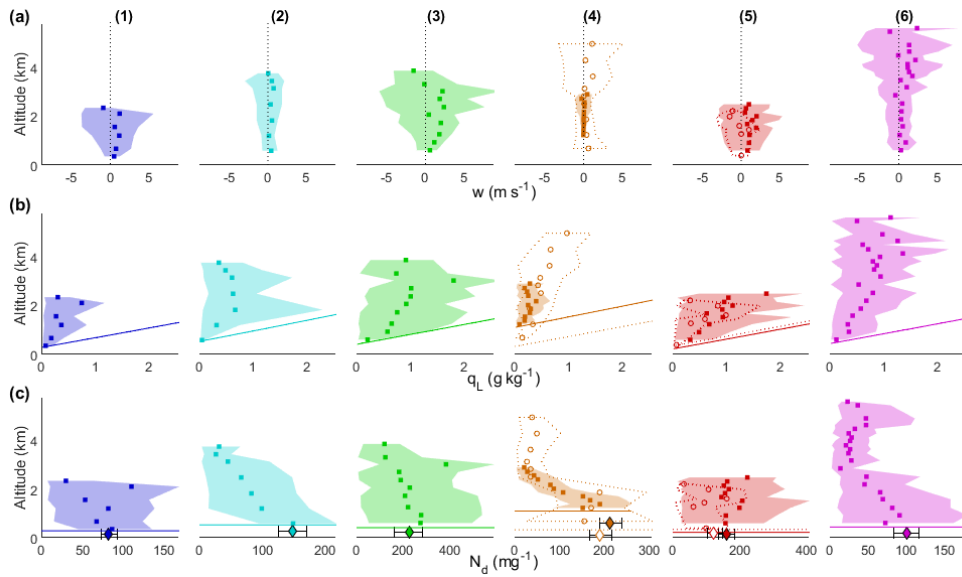


Figure 7: Statistics of in-cloud properties, measured in situ for Cases 1-6: (a) vertical velocity,  $w$ , (b) liquid water mixing ratio,  $q_L$ , (c) drop number concentration,  $N_d$ . The shaded region corresponds to the 10-90% range and dots are the transect mean values where data are filtered for cloud using  $q_L > 0.02 \text{ g kg}^{-1}$ . In the case of (a), the transect means are calculated as a  $q_L$ -weighted mean, referred to as  $w_L$  in the text. Also shown in (b) is an adiabatic parcel initialized from saturation at the lowest cloud base, shown as a horizontal line in (c). Also shown in (c) is a reference aerosol concentration based on the particle number concentration, exceeding 100 nm diameter, measured during sub-cloud sampling (marker: mean, bar: 10-90% range). In (4) and (5), data for the secondary modules are included (Case 4B and 5A, respectively) with dashed lines and open markers.



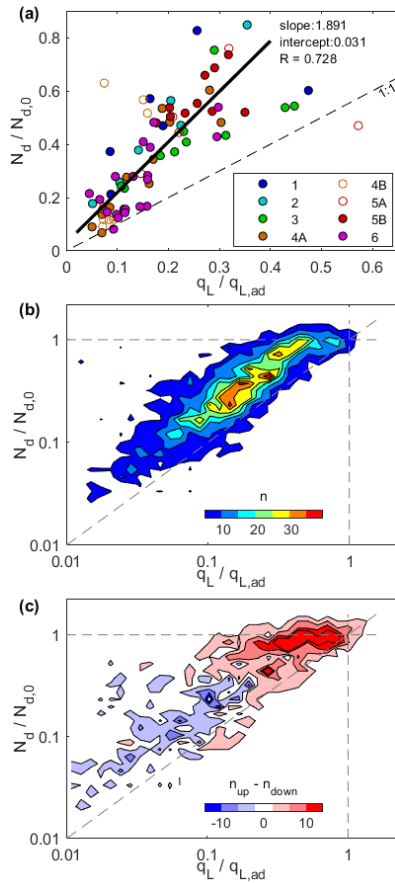


Figure 8: Variation of  $N_d$  and  $q_L$  with respect to a reference parcel with properties  $N_{d,0}$  and  $q_{L,ad}$ . (a) Transect in-cloud mean for Cases 1-6 (open circles for secondary modules). A linear model is fit to the data using total least squares with equal uncertainty in  $q_L$  and  $N_d$ . (b) Joint frequency distribution (counts,  $n$ ) of all cloudy data for all cases with logarithmically spaced bins. (c) Same as (b) but showing the difference in the joint frequency distribution between updrafts and downdrafts.

1285

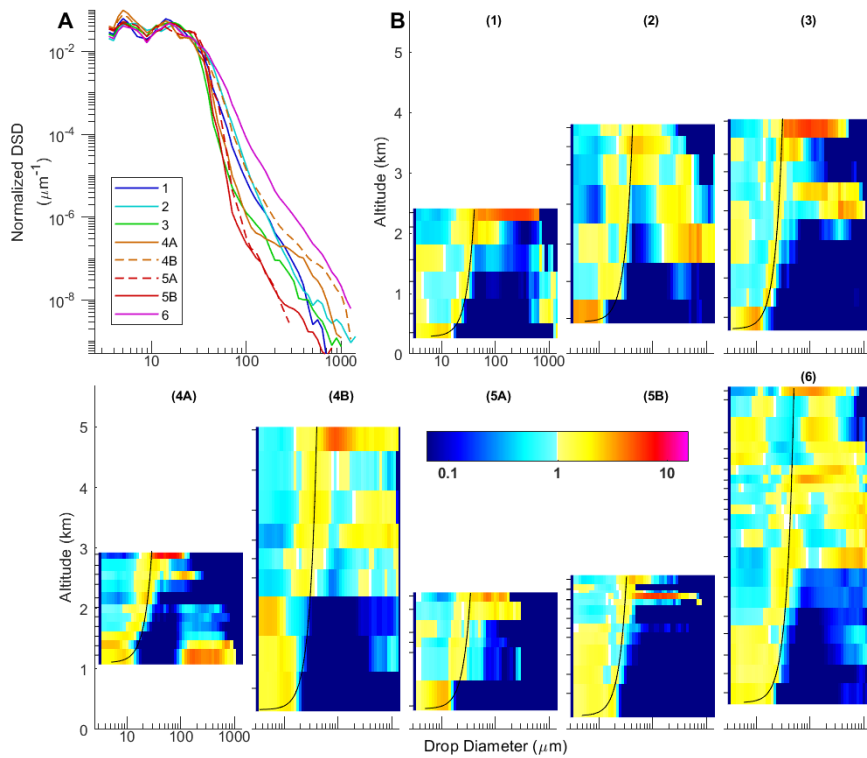
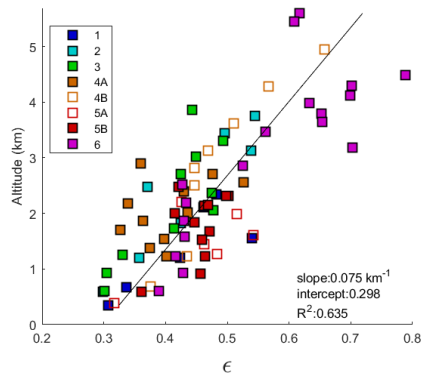


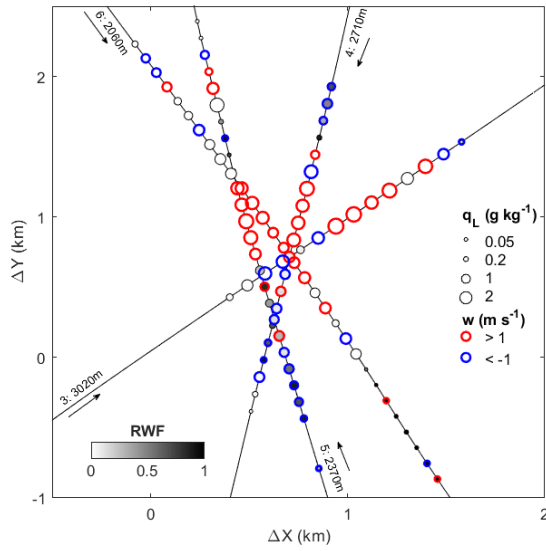
Figure 9: Vertical profile of the anomaly normalized drop size distributions (DSD). (A) Reference normalized DSD calculated from the mean across all levels sampled. (B) For Cases 1-6: At each level, the transect mean in-cloud DSD is normalized to unit integral, and then the anomaly is calculated as a ratio to the reference DSD. Warm (cold) colors therefore represent higher (lower) than average contribution to the DSD shape and use of the anomaly permits comparison across the size spectrum, despite the large change in concentration. Also shown for each case is the monodisperse drop diameter of an adiabatic parcel (black line) initialized at the lowest cloud base with a drop number concentration,  $N_0$  (see text).

1290

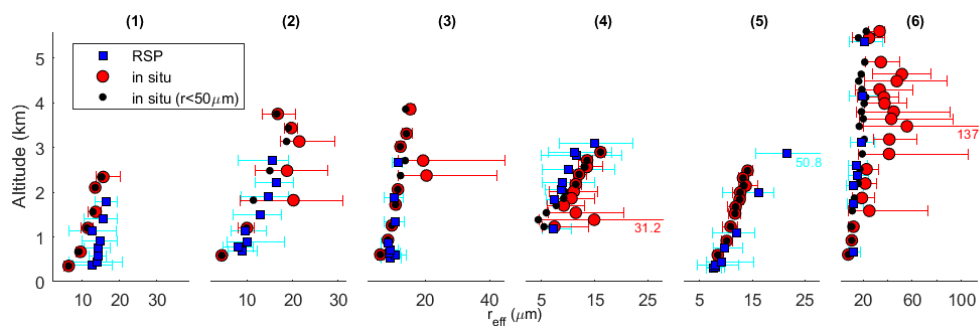


1295

Figure 10: Profiles of DSD relative dispersion,  $\epsilon$ , for Cases 1-6. Values of  $\epsilon$  are calculated locally at the measurement interval (1s,  $\sim 100$  m) and then averaged (weighted by  $N_d$ ) across a transect.



1300 Figure 11: Four sequential Falcon in situ transects (2-3 km altitude) through cloud during Case 3. The aircraft position has been projected onto a cloud-centric coordinate where X (Y) represents the displacement along (perpendicular to) the cluster motion. The size of the markers corresponds to the total  $q_L$  with shading indicating the rainwater fraction (RWF) defined as the fraction of  $q_L$  resulting from drop diameters exceeding 100  $\mu\text{m}$ . Red (blue) rings indicate updrafts (downdrafts).



1305

Figure 12: Comparison of the vertical profile of effective radius,  $r_{\text{eff}}$ , for Cases 1-6 between Falcon in situ cloud transects and composite profiles from RSP. The composite profiles were derived by grouping RSP retrievals into eight equal frequency bins of cloud top height as determined by HSRL, with the mean altitude of each bin displayed. A comparison is made with in situ derived  $r_{\text{eff}}$  omitting contributions from rain water ( $r < 50 \mu\text{m}$ ). For both datasets, the mean (markers) and 10-90% range

1310 (bars) are shown.

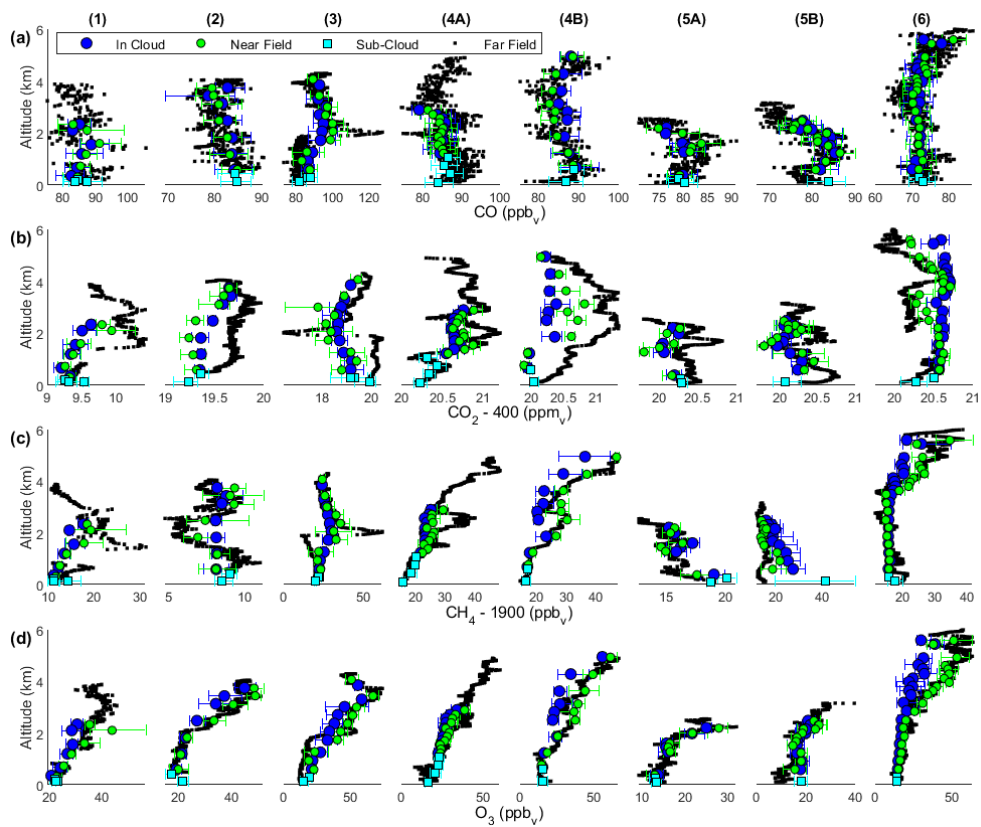


Figure 13: Trace gas vertical profiles separated into a far-field component measured during the Falcon clear spiral (black), a near-field component measured outside but in the vicinity of the cloud cluster at cloudy altitudes (green), an in-cloud component (blue), and a sub-cloud component (cyan). Data are shown for Cases 1-6 for (a) CO, (b) CO<sub>2</sub>, (c) CH<sub>4</sub>, and (d) O<sub>3</sub>. Note the changes in concentration scales.

1315

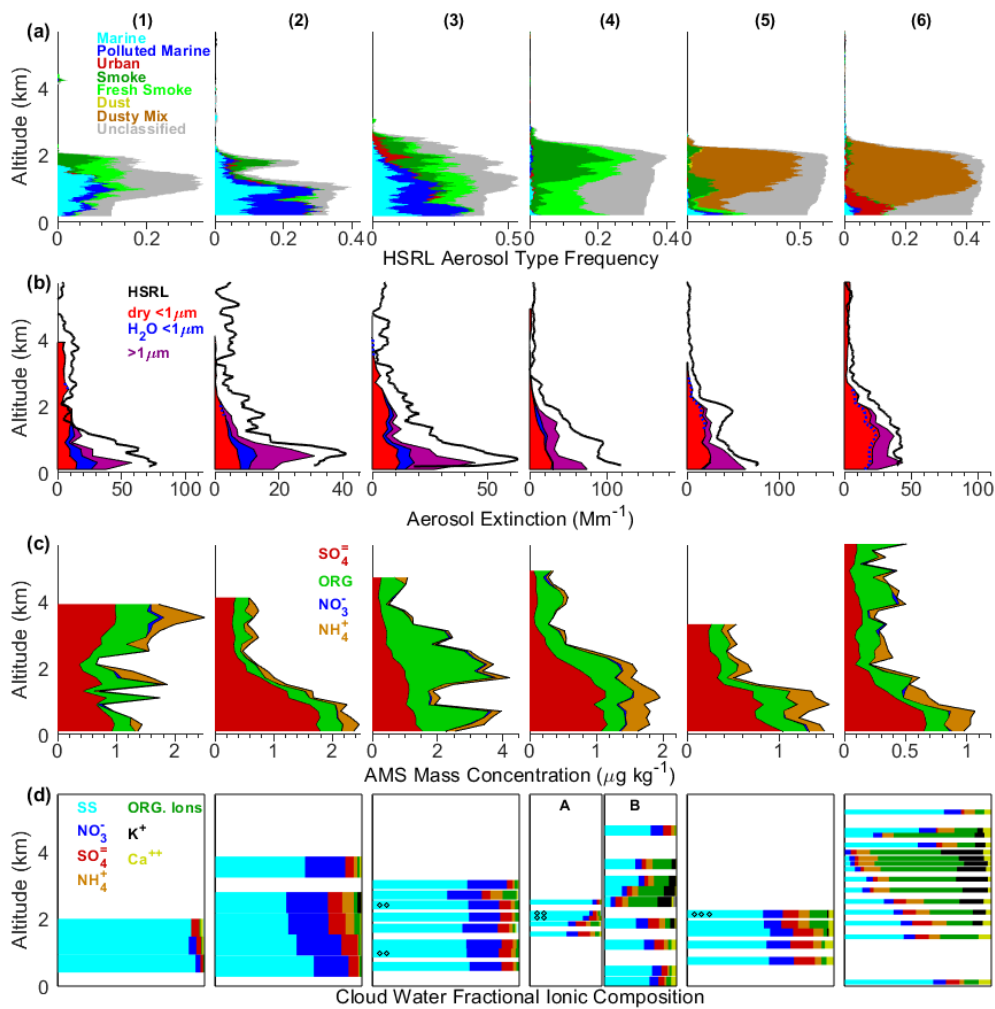
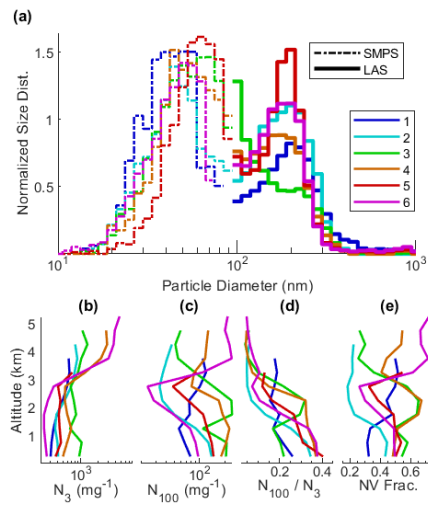


Figure 14: Vertical profiles of aerosol and cloud composition. (a) aerosol type frequency as derived by HSRL, (b) aerosol extinction components and comparison with HSRL, (c) aerosol sub-micrometer mass measured by the AMS, and (d) ionic composition of cloud water (note that no samples were captured during Case 5A and repeated samples at the same level are marked).

1320



1325 Figure 15: Aerosol microphysical properties for each case. (a) Normalized particle size distributions in the sub-cloud region, profiles of (b) total particle number concentration (>3 nm), (c) total particle number concentration (>100 nm), (d) the number fraction >100 nm, and (e) non-volatile number fraction (>10 nm).